

MHD-kinetic hybrid code based on structure-preserving finite elements with particles-in-cell

Florian Holderied^{1,2,*}, Stefan Possanner^{1,3}, and Xin Wang¹

¹*Max Planck Institute for Plasma Physics, Boltzmannstrasse 2, 85748 Garching, Germany*

²*Technical University of Munich, Department of Physics, James-Frank-Strasse 1, 85748 Garching, Germany*

³*Technical University of Munich, Department of Mathematics, Boltzmannstrasse 3, 85748 Garching, Germany*

* *Corresponding author: Florian Holderied, florian.holderied@ipp.mpg.de*

Abstract

We present a STRUcture-Preserving HYbrid code - STRUPHY - for the simulation of magneto-hydrodynamic (MHD) waves interacting with a population of energetic particles far from thermal equilibrium (kinetic species). The implemented model features linear, ideal MHD equations in curved, three-dimensional space, coupled nonlinearly to the full-orbit Vlasov equations via a current coupling scheme. The algorithm is based on finite element exterior calculus (FEEC) for MHD and particle-in-cell (PIC) methods for the kinetic part; it provably conserves mass, energy, and the divergence-free magnetic field, irrespective of metric (= space curvature), mesh parameters and chosen order of the scheme. These properties enable reliable long-time simulations of energetic particle physics in complex geometries, covering the whole range of MHD waves. In STRUPHY, the finite element spaces are built from tensor products of univariate B-splines on the logical cuboid and can be made high-order by increasing the polynomial degree. Time-stepping is based on Poisson splitting with implicit sub-steps, mitigating CFL conditions from fast magneto-acoustic waves. High-order time splitting schemes can be used in this regard.

1 Introduction

Plasma waves in magneto-hydrodynamic (MHD) fluids can be resonantly excited by energetic particles with thermal speeds in the range of the Alfvén velocity. Such wave-particle interactions are observed for instance in deuterium-tritium fusion reactors, where hot α -particles can destabilize shear Alfvén modes and thus compromise confinement time [20, 24, 11]. Another example is the interaction of energetic electrons in the solar wind with Whistler waves propagating in Earth’s magnetosphere. This interaction can lead to new types of electromagnetic waves whose spectrograms show discrete elements with rising or falling frequencies with respect to time (also known as frequency chirping) [35, 9, 30]. The associated nonlinear dynamics in realistic scenarios such as fusion reactors or solar wind can be studied via computer simulation of suitable model equations. The latter range from full kinetic models of all involved plasma species (bulk and energetic particles), over hybrid codes to reduced fluid simulations, all compared in a recent benchmark study [22]. The notion of a “hybrid code” implies the following two crucial features:

1. Use of reduced model equations for bulk plasma (for instance fluid instead of kinetic).
2. Fully self-consistent description of nonlinear dynamics (beyond the linear phase).

Examples of successful implementations of hybrid codes in fusion research are MEGA [32], M3D-K [5, 28], and HMGC [6, 36]. The appeal of hybrid codes is three-fold: a) reduced numerical cost compared to fully kinetic simulations, b) inclusion of non-equilibrium dynamics (wave-particle resonances)

compared to pure fluid simulations and c) possibility of direct comparison with analytic computations (for linear dynamics). The drawback is the increased complexity of model equations. For instance, while the geometric structure (i.e. Poisson bracket and/or variational principle) of MHD equations has been known for decades [27], the underlying structure of MHD-kinetic hybrid models has been discovered only very recently [33, 8]. This shows that the proper derivation of MHD-kinetic hybrids that respect fundamental physics principles such as energy conservation is a non-trivial task. As a consequence, little attention had been paid to these issues during the design of the first generation of hybrid codes mentioned above.

In parallel to the theoretical discoveries regarding hybrid models came the advent of geometric (or structure-preserving) methods for plasma equations, see [26] for a review. These methods obey many conservation properties implied by the geometric structure, such as conservation of energy, charge or momentum on the discrete level. The main idea is to discretize directly the underlying Poisson structure or variational principle, thus transferring geometric properties to a finite-dimensional setting. The very first structure-preserving geometric PIC algorithm was designed and implemented by Squire et al. in 2012 [31]. Similar methods have later been successfully applied to Vlasov-Maxwell [18, 29, 39, 38], Vlasov-Darwin [10] and Vlasov-Poisson equations [14, 37]. The first structure-preserving geometric PIC algorithm using finite element exterior calculus (FEEC) was designed by He et al. in 2016 [19]. The same approach has later been taken by Kraus et al. [23] who used B-spline basis functions to efficiently build the discrete de Rham complex, which contains Nédélec and Raviart-Thomas spaces. The theoretical foundation of FEEC has been laid by Arnold et al. [3, 1]; the interested reader may consult the recent book of Arnold [2] for a comprehensive overview.

In this work we apply the ideas of structure-preserving integration to a MHD-kinetic hybrid model, namely the Hamiltonian current-coupling (CC) scheme [33]. The equations consist of the three-dimensional, ideal MHD equations coupled to the collision-less, full-orbit Vlasov equation with three velocity degrees of freedom. The MHD part thus covers the entire set of MHD waves, namely shear Alfvén, slow- and fast magneto-acoustic waves. The kinetic equation contains the cyclotron motion of the energetic species, enabling the description of wave-particle resonances in this regime. The motivation for this work stems from the need of stable and reliable long-time simulations of energetic particle physics in tokamaks, stellarators and also space plasmas. In that regard, the version of STRUPHY presented in this paper can be viewed as the beginning of our quest to reach this goal by using the most modern numerical tools available, which ultimately will provide the necessary stability in nonlinear simulations. Future extensions of the code will feature also drift-kinetic or gyro-kinetic species, allowing for the efficient simulation of low-frequency phenomena.

In the current version of the code, we linearize the MHD part and focus on the nonlinear coupling to the kinetic species, which acts back on the bulk plasma via charge and current densities (CC). FEEC is used for the discretization of the MHD part and PIC for the kinetic part. The concept is similar to the GEMPIC-approach in [23], only that the role of the Maxwell equations is taken by the linear MHD equations. Another difference w.r.t. GEMPIC is that we discretize directly the equations rather than the variational principle or the Poisson bracket. There are three reasons for this: 1) linearized MHD equations lose their Hamiltonian structure if the magnetic background field is not chosen properly. In this case there is no such thing as a Poisson bracket or variational formulation, but our method of discretization still applies, 2) Poisson structures of extended hybrid models with two-fluid MHD, drift-kinetic or gyro-kinetic models are either not known or very cumbersome, such that pure "geometric" discretisation is not possible, and 3) we avoid a high level of abstraction in the presentation of the scheme. In fact, the mere existence of a Poisson structure on the continuous level is sufficient to translate several important conservation properties to the discrete level by applying FEEC to the equations directly. Our discretization of the CC hybrid models provably conserves energy, mass and the divergence-free magnetic field, irrespective of the metric, mesh parameters and chosen order of the scheme. This is thanks to the separation between topological and metric properties in the theory of differential forms, upon which FEEC is built, and due to the coupling with a particle-based kinetic solver. In STRUPHY, the finite element spaces are built from tensor products of univariate B-splines of arbitrary order, either periodic or clamped, on the logical cuboid. Position space is expressed in logical coordinates, also for the kinetic species, during the entire simulation. Results in physical space are

obtained in post-processing by a push-forward operation. The time stepping is implicit and based on Poisson-splitting of a skew-symmetric matrix. Most of the sub-steps are solved via the Crank-Nicolson method (average vector-field). Lie-Trotter and Strang splitting methods have been implemented, but higher-order methods would be in principle available [25].

This article is organized as follows. Section 2 first introduces the basic model equations along with some of its properties, followed by performing the linearisation of the MHD part. Subsequently, we derive the corresponding model equations in curvilinear coordinates and in terms of differential forms in order to prepare the application of FEEC. Based on these results, Section 3 describes in detail the spatial discretization, followed by a discussion of some properties of the resulting semi-discrete system of ordinary differential equations with continuous time variable. We also review the realization of the compatible finite element spaces along with projection operators on these spaces using B-spline basis functions. Section 4 is devoted to the proposed time integration scheme based on Poisson splitting. Numerical results are shown in Section 5 before we summarize and conclude in Section 6. Additionally, this article contains three appendices. Appendix A contains formulae for the exterior calculus of differential forms including transformation formulae between vector/scalar fields and differential forms. While we focus on the full- f method in the main text, Appendix B outlines the modifications that have to be made if the δf method is used. Finally, Appendix C contains two tables completing Section 3.4.2.

2 Model equations

2.1 Hamiltonian current coupling

Our target model is a MHD-kinetic hybrid model in which the coupling between fluid bulk and kinetic species (subscript "h" for "hot") appears through the Lorentz force terms. This is called current-coupling (CC) and involves the first two moments of the kinetic species' distribution function f_h , namely the charge density $\rho_h = \rho_h(t, \mathbf{x})$ and the current density $\mathbf{J}_h = \mathbf{J}_h(t, \mathbf{x})$. Denoting by $\nabla = (\partial_x, \partial_y, \partial_z)^\top$ and $\nabla_{\mathbf{v}} = (\partial_{v_x}, \partial_{v_y}, \partial_{v_z})^\top$ the nabla-operator acting on spatial and velocity coordinates, respectively, the Hamiltonian CC in SI-units reads [33]

$$\text{MHD} \quad \begin{cases} \frac{\partial \rho}{\partial t} + \nabla \cdot (\rho \mathbf{U}) = 0, \\ \rho \left[\frac{\partial \mathbf{U}}{\partial t} + (\mathbf{U} \cdot \nabla) \mathbf{U} \right] + \nabla p = \rho_h (\mathbf{U} \times \mathbf{B}) + \left(\frac{\nabla \times \mathbf{B}}{\mu_0} - \mathbf{J}_h \right) \times \mathbf{B}, \\ \frac{\partial p}{\partial t} + \nabla \cdot (p \mathbf{U}) + (\gamma - 1) p \nabla \cdot \mathbf{U} = 0, \\ \frac{\partial \mathbf{B}}{\partial t} = \nabla \times (\mathbf{U} \times \mathbf{B}), \end{cases} \quad (2.1a)$$

$$\text{kinetics} \quad \begin{cases} \frac{\partial f_h}{\partial t} + \mathbf{v} \cdot \nabla f_h + \frac{q_h}{m_h} (\mathbf{B} \times \mathbf{U} + \mathbf{v} \times \mathbf{B}) \cdot \nabla_{\mathbf{v}} f_h = 0, \\ \rho_h = q_h \int_{\mathbb{R}^3} f_h d^3v, \quad \mathbf{J}_h = q_h \int_{\mathbb{R}^3} \mathbf{v} f_h d^3v, \end{cases} \quad (2.1b)$$

supplemented to the zero-divergence constraint $\nabla \cdot \mathbf{B} = 0$. This set of equations forms a closed system of nonlinear partial differential equations describing the time evolution of the mass density $\rho = \rho(t, \mathbf{x})$, mean velocity $\mathbf{U} = \mathbf{U}(t, \mathbf{x})$, pressure $p = p(t, \mathbf{x})$, magnetic flux density $\mathbf{B} = \mathbf{B}(t, \mathbf{x})$ (which we will simply refer to as magnetic field) and hot ion distribution function $f_h = f_h(t, \mathbf{x}, \mathbf{v})$. The system is defined for times $t \in \mathbb{R}_0^+$ in a domain $\Omega \subset \mathbb{R}^3$ with smooth boundary $\partial\Omega$ and supplemented with suitable initial and boundary conditions. Furthermore, $\gamma = 5/3$ is the heat capacity ratio of an ideal gas and μ_0 denotes the vacuum permeability, q_h the kinetic species' charge¹ and m_h its mass. The model is based on common assumptions made in MHD:

1. Quasi-neutrality (the total charge density $\rho_c \rightarrow 0$),

¹We assume kinetic ions with positive charge.

2. Characteristic velocities well-below the speed of light ($|\mathbf{U}| \ll c$),
3. Negligence of electron inertia ($m_e \rightarrow 0$),
4. Ohm's law of the form $\mathbf{E} = -\mathbf{U} \times \mathbf{B}$ (*ideal* MHD: plasma resistivity $\sigma \rightarrow 0$).

In the following we set μ_0 , q_h and m_h to one for better readability.

The system (2.1) possesses a noncanonical Hamiltonian structure, i.e. it can be derived from a Poisson bracket together with the conserved Hamiltonian

$$\mathcal{H}_0(t) = \frac{1}{2} \int_{\Omega} \rho \mathbf{U}^2 d^3x + \frac{1}{\gamma - 1} \int_{\Omega} p d^3x + \frac{1}{2} \int_{\Omega} \mathbf{B}^2 d^3x + \frac{1}{2} \int_{\Omega} \int_{\mathbb{R}^3} \mathbf{v}^2 f_h d^3v d^3x, \quad (2.2)$$

which is equal to the total energy of the system. Other conserved quantities are the total mass, momentum and the magnetic helicity

$$M(t) = \int_{\Omega} \rho d^3x + \int_{\Omega} \int_{\mathbb{R}^3} f_h d^3v d^3x, \quad (2.3)$$

$$\mathbf{P}(t) = \int_{\Omega} \rho \mathbf{U} d^3x + \int_{\Omega} \int_{\mathbb{R}^3} \mathbf{v} f_h d^3v d^3x, \quad (2.4)$$

$$H_m(t) = \int_{\Omega} \mathbf{A} \cdot \mathbf{B} d^3x, \quad (2.5)$$

where \mathbf{A} is the magnetic vector potential from which the magnetic field is obtained by $\mathbf{B} = \nabla \times \mathbf{A}$.

2.2 Linearization of the MHD part

In this work we consider CC with linearized MHD. This is sufficient for describing the three fundamental types of waves in ideal MHD, that are, the slow and fast magnetosonic wave and the shear Alfvén wave. Assuming that MHD waves are small perturbations (denoted by tildes) with respect to a pre-defined equilibrium state (denoted by the subscript "eq") satisfying the condition $\nabla p_{\text{eq}} = (\nabla \times \mathbf{B}_{\text{eq}} - \mathbf{J}_{h,\text{eq}}) \times \mathbf{B}_{\text{eq}}$, we make the ansatzes $\rho = \rho_{\text{eq}} + \tilde{\rho}$, $\mathbf{U} = \tilde{\mathbf{U}}$ (zero-flow equilibrium), $p = p_{\text{eq}} + \tilde{p}$ and $\mathbf{B} = \mathbf{B}_{\text{eq}} + \tilde{\mathbf{B}}$ for the MHD variables, plug it in (2.1a) and neglect all nonlinear terms except for the ones involving the kinetic particles. Hence we keep nonlinear coupling terms between the fluid and kinetic species. The partially linearized model then reads

$$\text{MHD} \quad \left\{ \begin{array}{l} \frac{\partial \tilde{\rho}}{\partial t} + \nabla \cdot (\rho_{\text{eq}} \tilde{\mathbf{U}}) = 0, \\ \rho_{\text{eq}} \frac{\partial \tilde{\mathbf{U}}}{\partial t} + \nabla \tilde{p} = (\nabla \times \tilde{\mathbf{B}}) \times \mathbf{B}_{\text{eq}} + (\nabla \times \mathbf{B}_{\text{eq}}) \times \tilde{\mathbf{B}} + (\rho_h \tilde{\mathbf{U}} - \mathbf{J}_h) \times \mathbf{B}, \\ \frac{\partial \tilde{p}}{\partial t} + \nabla \cdot (p_{\text{eq}} \tilde{\mathbf{U}}) + (\gamma - 1) p_{\text{eq}} \nabla \cdot \tilde{\mathbf{U}} = 0, \\ \frac{\partial \tilde{\mathbf{B}}}{\partial t} = \nabla \times (\tilde{\mathbf{U}} \times \mathbf{B}_{\text{eq}}), \end{array} \right. \quad (2.6a)$$

$$\text{kinetics} \quad \left\{ \begin{array}{l} \frac{\partial f_h}{\partial t} + \mathbf{v} \cdot \nabla f_h + (\mathbf{B} \times \tilde{\mathbf{U}} + \mathbf{v} \times \mathbf{B}) \cdot \nabla_v f_h = 0, \\ \rho_h = \int_{\mathbb{R}^3} f_h d^3v, \quad \mathbf{J}_h = \int_{\mathbb{R}^3} \mathbf{v} f_h d^3v. \end{array} \right. \quad (2.6b)$$

The linearization of the MHD part has the consequence that the original Hamiltonian (2.2) is no longer conserved. However, the quantity

$$\mathcal{H}_1(t) = \frac{1}{2} \int_{\Omega} \rho_{\text{eq}} \tilde{\mathbf{U}}^2 d^3x + \frac{1}{\gamma - 1} \int_{\Omega} \tilde{p} d^3x + \frac{1}{2} \int_{\Omega} \tilde{\mathbf{B}}^2 d^3x + \frac{1}{2} \int_{\Omega} \int_{\mathbb{R}^3} \mathbf{v}^2 f_h d^3v d^3x, \quad (2.7)$$

evolves in time as

$$\frac{d\mathcal{H}_1}{dt} = \int_{\Omega} \tilde{\mathbf{U}} \cdot [(\nabla \times \mathbf{B}_{\text{eq}}) \times \tilde{\mathbf{B}}] d^3x - \int_{\Omega} (p_{\text{eq}} - \tilde{p}) \nabla \cdot \tilde{\mathbf{U}} d^3x, \quad (2.8)$$

Scalar fields $\hat{a} = \hat{a}(\boldsymbol{\eta})$ and vector fields $\mathbf{a} \in T\Omega^3$ with components $\hat{\mathbf{a}} = \hat{\mathbf{a}}(\boldsymbol{\eta})$ can be related to differential p -forms $a^p \in \Lambda^p(\Omega) : T\Omega \times \dots \times T\Omega \rightarrow \mathbb{R}$, $p \in \{0, 1, 2, 3\}$ with components $\hat{\mathbf{a}}^p = \hat{\mathbf{a}}^p(\boldsymbol{\eta})$ in the following way:

$$a^0 = \hat{a}^0, \quad \Leftrightarrow \quad \hat{a}^0 = \hat{a}, \quad (2.13a)$$

$$a^1 = \hat{a}_1^1 d\eta^1 + \hat{a}_2^1 d\eta^2 + \hat{a}_3^1 d\eta^3, \quad \Leftrightarrow \quad \hat{\mathbf{a}}^1 = \begin{pmatrix} \hat{a}_1^1 \\ \hat{a}_2^1 \\ \hat{a}_3^1 \end{pmatrix} = G\hat{\mathbf{a}}, \quad (2.13b)$$

$$a^2 = \hat{a}_1^2 (d\eta^2 \wedge d\eta^3) + \hat{a}_2^2 (d\eta^3 \wedge d\eta^1) + \hat{a}_3^2 (d\eta^1 \wedge d\eta^2), \quad \Leftrightarrow \quad \hat{\mathbf{a}}^2 = \begin{pmatrix} \hat{a}_1^2 \\ \hat{a}_2^2 \\ \hat{a}_3^2 \end{pmatrix} = \sqrt{g}\hat{\mathbf{a}}, \quad (2.13c)$$

$$a^3 = \hat{a}^3 (d\eta^1 \wedge d\eta^2 \wedge d\eta^3), \quad \Leftrightarrow \quad \hat{\mathbf{a}}^3 = \sqrt{g}\hat{\mathbf{a}}. \quad (2.13d)$$

The right-hand side of (2.13b) is the defining relation for the *sharp*-operator

$$\sharp : \Lambda^1(\Omega) \rightarrow T\Omega, \quad \hat{\mathbf{a}}^1 \mapsto G^{-1}\hat{\mathbf{a}}^1 = \hat{\mathbf{a}}, \quad (2.14)$$

which transforms a differential 1-form to a vector field. In (2.13b), $d\eta^\mu$ ($\mu \in \{1, 2, 3\}$) are the lines of the inverse Jacobian matrix DF^{-1} . They represent the *covariant* basis vectors which span the cotangent space $T_x^*\Omega$ at $\mathbf{x} \in \Omega$, that is, the dual space of $T_x\Omega$. The elements of $T_x^*\Omega$ are called 1-forms. Higher-order forms are constructed via the wedge product \wedge (see A.1). 0-forms are just functions on the logical domain. Let us summarize some notations regarding scalar fields, vector fields and p -forms:

- a and \mathbf{a} denote scalar fields and components of vector fields in Cartesian (physical) coordinates, respectively.
- \hat{a} and $\hat{\mathbf{a}}$ denote scalar fields and components of vector fields in curvilinear (logical) coordinates, respectively.
- a^p for $p \in \{0, 1, 2, 3\}$ denotes a differential p -form.
- \hat{a}^p for $p \in \{0, 3\}$ denotes the component of a 0- and 3-form, respectively.
- $\hat{\mathbf{a}}^p$ for $p \in \{1, 2\}$ denotes the components of a 1- and 2-form, respectively.
- As in (2.13), we use the symbol \Leftrightarrow to relate a p -form to its components, e.g. $a^1 \Leftrightarrow \hat{\mathbf{a}}^1$.

A p -form can be integrated over a p -dimensional manifold. This can give some guidance of how to choose the appropriate degree of a form for a physical unknown (a flux for instance, which is usually integrated over a surface, would correspond to a 2-form). But this choice is not mandatory, as a p -form can be transformed to $(3-p)$ -forms by means of the Hodge-star operator $*$ (see (A.3)). Hence there are many ways of how to write (2.12) or (2.6a) in terms of differential forms. The choice can be made for purely numerical reasons, such as the implementation of boundary conditions. In this work we are guided by two main principles:

1. Keep the "frozen-in" (to the fluid velocity \mathbf{U}) equations for the mass density ρ and the magnetic field \mathbf{B} in strong form in order to achieve strong conservation of mass and $\nabla \cdot \mathbf{B} = 0$ on the discrete level.
2. Write the momentum conservation law in the weak form to accommodate for the coupling to the particles via Monte-Carlo integration.

³ $T\Omega$ denotes the tangent bundle, that is, the union of all tangent spaces $T_x\Omega$, $\forall \mathbf{x} \in \Omega$.

The first point leads to ρ being a 3-form and to \mathbf{B} being a 2-form. Moreover, we choose \mathbf{U} as a 1-form and the pressure p as a 0-form.

Upon multiplying (2.12a) with \sqrt{g} , (2.12b) from the left-hand side with DF^\top and (2.12d) again from the left-hand side with $DF^{-1}\sqrt{g}$, respectively, and applying the relations between scalar fields and components of vector fields to components of differential forms (2.13), we obtain the following system for the components of the respective forms:

$$\left\{ \begin{array}{l} \frac{\partial \hat{\rho}^3}{\partial t} + \hat{\nabla} \cdot (\hat{\rho}_{\text{eq}}^3 G^{-1} \hat{\mathbf{U}}^1) = 0, \end{array} \right. \quad (2.15a)$$

$$\left\{ \begin{array}{l} \frac{\hat{\rho}_{\text{eq}}^3}{\sqrt{g}} \frac{\partial \hat{\mathbf{U}}^1}{\partial t} + \hat{\nabla} \hat{p}^0 = \left[\hat{\nabla} \times \left(\frac{1}{\sqrt{g}} G \hat{\mathbf{B}}^2 \right) \right] \times \left(\frac{1}{\sqrt{g}} \hat{\mathbf{B}}_{\text{eq}}^2 \right) + \left[\hat{\nabla} \times \left(\frac{1}{\sqrt{g}} G \hat{\mathbf{B}}_{\text{eq}}^2 \right) \right] \times \left(\frac{1}{\sqrt{g}} \hat{\mathbf{B}}^2 \right) \\ \quad - \frac{\hat{\rho}_{\text{h}}^3}{\sqrt{g}} \left(\hat{\mathbf{B}}_{\text{f}}^2 \times G^{-1} \hat{\mathbf{U}}^1 \right) + \frac{1}{\sqrt{g}} \left(\hat{\mathbf{B}}_{\text{f}}^2 \times \hat{\mathbf{J}}_{\text{h}}^2 \right), \end{array} \right. \quad (2.15b)$$

$$\left\{ \begin{array}{l} \frac{\partial \hat{p}^0}{\partial t} + \frac{1}{\sqrt{g}} \hat{\nabla} \cdot \left(\sqrt{g} \hat{p}_{\text{eq}}^0 G^{-1} \hat{\mathbf{U}}^1 \right) + (\gamma - 1) \hat{p}_{\text{eq}}^0 \frac{1}{\sqrt{g}} \hat{\nabla} \cdot \left(\sqrt{g} G^{-1} \hat{\mathbf{U}}^1 \right) = 0, \end{array} \right. \quad (2.15c)$$

$$\left\{ \begin{array}{l} \frac{\partial \hat{\mathbf{B}}^2}{\partial t} = \hat{\nabla} \times \left(G^{-1} \hat{\mathbf{U}}^1 \times \hat{\mathbf{B}}_{\text{eq}}^2 \right). \end{array} \right. \quad (2.15d)$$

The MHD equations (2.15) in terms of components of differential forms are the basis of the discretization presented in this work. Note in particular the absence the Jacobian \sqrt{g} in front of the divergence and curl operators in (2.15a) and (2.15d), respectively, a fact which allows us to translate mass conservation and $\nabla \cdot \mathbf{B} = 0$ to the discrete level exactly (they become topological properties, independent of grid spacing and metric). Using $d^3x = \sqrt{g} d^3\eta$ which is essentially the transformation (2.13d), the MHD part of the energy (2.7) in terms of components of forms is given by

$$\mathcal{H}_{1,\text{MHD}}(t) = \frac{1}{2} \int_{\hat{\Omega}} (\hat{\mathbf{U}}^1)^\top G^{-1} \hat{\mathbf{U}}^1 \sqrt{g} d^3\eta + \frac{1}{2} \int_{\hat{\Omega}} (\hat{\mathbf{B}}^2)^\top G \hat{\mathbf{B}}^2 \frac{1}{\sqrt{g}} d^3\eta + \frac{1}{\gamma - 1} \int_{\hat{\Omega}} \hat{p}^0 \sqrt{g} d^3\eta. \quad (2.16)$$

Finally, we can write (2.15) in a coordinate-free representation with additional operators known from differential geometry, such as the interior product (A.2) and the exterior derivative d (Table 2):

$$\frac{\partial \rho^3}{\partial t} + d(i_{\#U^1} \rho_{\text{eq}}^3) = 0, \quad (2.17a)$$

$$(*\rho_{\text{eq}}^3) \wedge \frac{\partial U^1}{\partial t} + dp^0 = i_{\#*B_{\text{eq}}^2} d * B^2 + i_{\#*B^2} d * B_{\text{eq}}^2 - (*\rho_{\text{h}}^3) \wedge (i_{\#U^1} B_{\text{f}}^2) + i_{\#*J_{\text{h}}^2} B_{\text{f}}^2, \quad (2.17b)$$

$$\frac{\partial p^0}{\partial t} - d^*(p_{\text{eq}}^0 \wedge U^1) - (\gamma - 1) p_{\text{eq}}^0 \wedge d^* U^1 = 0, \quad (2.17c)$$

$$\frac{\partial B^2}{\partial t} + d(i_{\#U^1} B_{\text{eq}}^2) = 0. \quad (2.17d)$$

The *co-differential* operator d^* is defined in (A.10). As shown in Table 2, the exterior derivative d acts on a 0-form as the usual grad operator on a scalar field in Cartesian coordinates. In the same way, d acts on the components of a 1-form and 2-form as the curl and div operators on components of a vector field in Cartesian coordinates, respectively.

3 Semi-discretization in space

3.1 Commuting diagram and finite element spaces

We perform the spatial discretization of (2.15) using the framework of Finite Element Exterior Calculus (FEEC) to derive a semi-discrete system of ordinary differential equations with continuous time variable. At the heart of FEEC is the commuting diagram for function spaces depicted in Figure

$$\begin{array}{ccccccc}
H^1(\hat{\Omega}) & \xrightarrow{\hat{\nabla}} & H(\text{curl}, \hat{\Omega}) & \xrightarrow{\hat{\nabla} \times} & H(\text{div}, \hat{\Omega}) & \xrightarrow{\hat{\nabla} \cdot} & L^2(\hat{\Omega}) \\
\Pi_0 \downarrow & & \Pi_1 \downarrow & & \Pi_2 \downarrow & & \Pi_3 \downarrow \\
V_0 & \xrightarrow{\hat{\nabla}} & V_1 & \xrightarrow{\hat{\nabla} \times} & V_2 & \xrightarrow{\hat{\nabla} \cdot} & V_3
\end{array}$$

Figure 1: Commuting diagram for function spaces in three space dimensions. The upper line represents the continuous, infinite-dimensional function spaces for components of p -forms (3.1) and the lower line finite-dimensional sub-spaces V_0, V_1, V_2 and V_3 . Due to the properties $\text{curl}(\text{grad}) = 0$ and $\text{div}(\text{curl}) = 0$, both lines form an exact de Rham sequence. The link between the two sequences is made by the projection operators $\Pi_0 : H^1(\hat{\Omega}) \rightarrow V_0$, $\Pi_1 : H(\text{curl}, \hat{\Omega}) \rightarrow V_1$, $\Pi_2 : H(\text{div}, \hat{\Omega}) \rightarrow V_2$ and $\Pi_3 : L^2(\hat{\Omega}) \rightarrow V_3$ onto the finite element spaces. They must be constructed in a way that the diagram becomes commuting.

1. Note that all spaces in the diagram are spaces of the components of differential forms **which are independent of the basis forms**. The infinite-dimensional spaces in the upper line are defined as

$$H^1(\hat{\Omega}) := \{\hat{a}^0 : \hat{\Omega} \rightarrow \mathbb{R}, \quad \hat{a}^0 \leftrightarrow a^0 \quad \text{s.t.} \quad (a^0, a^0) + (da^0, da^0) < \infty\}, \quad (3.1a)$$

$$H(\text{curl}, \hat{\Omega}) := \{\hat{\mathbf{a}}^1 : \hat{\Omega} \rightarrow \mathbb{R}^3, \quad \hat{\mathbf{a}}^1 \leftrightarrow a^1 \quad \text{s.t.} \quad (a^1, a^1) + (da^1, da^1) < \infty\}, \quad (3.1b)$$

$$H(\text{div}, \hat{\Omega}) := \{\hat{\mathbf{a}}^2 : \hat{\Omega} \rightarrow \mathbb{R}^3, \quad \hat{\mathbf{a}}^2 \leftrightarrow a^2 \quad \text{s.t.} \quad (a^2, a^2) + (da^2, da^2) < \infty\}, \quad (3.1c)$$

$$L^2(\hat{\Omega}) := \{\hat{a}^3 : \hat{\Omega} \rightarrow \mathbb{R}, \quad \hat{a}^3 \leftrightarrow a^3 \quad \text{s.t.} \quad (a^3, a^3) < \infty\}, \quad (3.1d)$$

where the action of the exterior derivative d is summarized in Table 2 and the scalar product (a^p, a^p) of p -forms is defined in (A.6). We note two important properties of the diagram:

1. Exact sequence both on the continuous and the discrete level:

$$\hat{\nabla} V_0 = \text{Ker}(\hat{\nabla} \times V_1), \quad \hat{\nabla} \times V_1 = \text{Ker}(\hat{\nabla} \cdot V_2), \quad (3.2)$$

2. Commutativity:

$$\Pi_1(\hat{\nabla} \hat{a}^0) = \hat{\nabla}(\Pi_0 \hat{a}^0), \quad \Pi_2(\hat{\nabla} \times \hat{\mathbf{a}}^1) = \hat{\nabla} \times (\Pi_1 \hat{\mathbf{a}}^1), \quad \Pi_3(\hat{\nabla} \cdot \hat{\mathbf{a}}^2) = \hat{\nabla} \cdot (\Pi_2 \hat{\mathbf{a}}^2). \quad (3.3)$$

The first property mimics the operator identities $\text{curl}(\text{grad}) = 0$ and $\text{div}(\text{curl}) = 0$ from the continuous level.

There are multiple ways how to construct the sequence of finite element spaces V_0, V_1, V_2 and V_3 forming an exact de Rham sequence. In this work, we shall do this by means of tensor-products of univariate B-spline basis functions introduced in [7]. We recall the construction of the spaces along with commuting projection operators in Section 3.4. We denote the total number of basis functions in each space by N^n with $n \in \{0, 1, 2, 3\}$ and the number of basis functions for each component of the two vector-valued spaces by N_μ^n for $n \in \{1, 2\}$ and $\mu = \{1, 2, 3\}$ such that $N^n = N_1^n + N_2^n + N_3^n$ for $n \in \{1, 2\}$. This yields the following finite element spaces and approximate components of forms,

denoted by the subscript h :

$$V_0 := \text{span} \{ \Lambda_i^0 \mid 0 \leq i < N^0 \}, \quad \hat{p}_h^0(t, \boldsymbol{\eta}) = \sum_{i=0}^{N^0-1} p_i(t) \Lambda_i^0(\boldsymbol{\eta}), \quad (3.4a)$$

$$V_1 := \text{span} \left\{ \left(\begin{array}{c} \Lambda_{1,i}^1 \\ 0 \\ 0 \end{array} \right), \left(\begin{array}{c} 0 \\ \Lambda_{2,i}^1 \\ 0 \end{array} \right), \left(\begin{array}{c} 0 \\ 0 \\ \Lambda_{3,i}^1 \end{array} \right) \mid \begin{array}{l} 0 \leq i < N_1^1 \\ 0 \leq i < N_2^1 \\ 0 \leq i < N_3^1 \end{array} \right\}, \quad \hat{U}_h^1(t, \boldsymbol{\eta}) = \sum_{\mu=1}^3 \sum_{i=0}^{N_\mu^1-1} u_{\mu,i}(t) \Lambda_{\mu,i}^1(\boldsymbol{\eta}) \mathbf{e}_\mu, \quad (3.4b)$$

$$V_2 := \text{span} \left\{ \left(\begin{array}{c} \Lambda_{1,i}^2 \\ 0 \\ 0 \end{array} \right), \left(\begin{array}{c} 0 \\ \Lambda_{2,i}^2 \\ 0 \end{array} \right), \left(\begin{array}{c} 0 \\ 0 \\ \Lambda_{3,i}^2 \end{array} \right) \mid \begin{array}{l} 0 \leq i < N_1^2 \\ 0 \leq i < N_2^2 \\ 0 \leq i < N_3^2 \end{array} \right\}, \quad \hat{B}_h^2(t, \boldsymbol{\eta}) = \sum_{\mu=1}^3 \sum_{i=0}^{N_\mu^2-1} b_{\mu,i}(t) \Lambda_{\mu,i}^2(\boldsymbol{\eta}) \mathbf{e}_\mu, \quad (3.4c)$$

$$V_3 := \text{span} \{ \Lambda_i^3 \mid 0 \leq i < N^3 \}, \quad \hat{\rho}_h^3(t, \boldsymbol{\eta}) = \sum_{i=0}^{N^3-1} \rho_i(t) \Lambda_i^3(\boldsymbol{\eta}). \quad (3.4d)$$

Here, $\mathbf{e}_1 = (1, 0, 0)^\top$, $\mathbf{e}_2 = (0, 1, 0)^\top$ and $\mathbf{e}_3 = (0, 0, 1)^\top$. To simplify the notation, we stack the finite element coefficients and basis functions in column vectors, e.g. $\mathbf{p} := (\hat{p}_i)_{0 \leq i < N^0} \in \mathbb{R}^{N^0}$ and $\boldsymbol{\Lambda}^0 := (\Lambda_i^0)_{0 \leq i < N^0} \in \mathbb{R}^{N^0}$. The right-hand sides of (3.4) can then compactly written as

$$\hat{p}_h^0 = (p, \dots, p_{N^0-1}) \begin{pmatrix} \Lambda_0^0 \\ \vdots \\ \Lambda_{N^0-1}^0 \end{pmatrix} =: \mathbf{p}^\top \boldsymbol{\Lambda}^0, \quad (3.5a)$$

$$(\hat{U}_h^1)^\top = \underbrace{(u_{1,0}, \dots, u_{1,N_1^1-1})}_{=: \mathbf{u}_1^\top} \underbrace{(u_{2,0}, \dots, u_{2,N_2^1-1})}_{=: \mathbf{u}_2^\top} \underbrace{(u_{3,0}, \dots, u_{3,N_3^1-1})}_{=: \mathbf{u}_3^\top} \begin{pmatrix} \boldsymbol{\Lambda}_1^1 & 0 & 0 \\ 0 & \boldsymbol{\Lambda}_2^1 & 0 \\ 0 & 0 & \boldsymbol{\Lambda}_3^1 \end{pmatrix} =: \mathbf{u}^\top \boldsymbol{\Lambda}^1, \quad (3.5b)$$

$$(\hat{B}_h^2)^\top = \underbrace{(b_{1,0}, \dots, b_{1,N_1^2-1})}_{=: \mathbf{b}_1^\top} \underbrace{(b_{2,0}, \dots, b_{2,N_2^2-1})}_{=: \mathbf{b}_2^\top} \underbrace{(b_{3,0}, \dots, b_{3,N_3^2-1})}_{=: \mathbf{b}_3^\top} \begin{pmatrix} \boldsymbol{\Lambda}_1^2 & 0 & 0 \\ 0 & \boldsymbol{\Lambda}_2^2 & 0 \\ 0 & 0 & \boldsymbol{\Lambda}_3^2 \end{pmatrix} =: \mathbf{b}^\top \boldsymbol{\Lambda}^2, \quad (3.5c)$$

$$\hat{\rho}_h^3 = (\rho_0, \dots, \rho_{N^3-1}) \begin{pmatrix} \Lambda_0^3 \\ \vdots \\ \Lambda_{N^3-1}^3 \end{pmatrix} =: \boldsymbol{\rho}^\top \boldsymbol{\Lambda}^3, \quad (3.5d)$$

such that $\boldsymbol{\Lambda}^1 \in \mathbb{R}^{N^1 \times 3}$ and $\boldsymbol{\Lambda}^2 \in \mathbb{R}^{N^2 \times 3}$. Moreover, we introduce discrete representations of the exterior derivative which are matrices solely acting on finite element coefficients, e.g.

$$\hat{\nabla} \hat{p}_h^0 = (\mathbb{G}\mathbf{p})^\top \boldsymbol{\Lambda}^1, \quad \hat{\nabla} \times \hat{U}_h^1 = (\mathbb{C}\mathbf{u})^\top \boldsymbol{\Lambda}^2, \quad \hat{\nabla} \cdot \hat{B}_h^2 = (\mathbb{D}\mathbf{b})^\top \boldsymbol{\Lambda}^3, \quad (3.6)$$

where $\mathbb{G} \in \mathbb{R}^{N^1 \times N^0}$, $\mathbb{C} \in \mathbb{R}^{N^2 \times N^1}$ and $\mathbb{D} \in \mathbb{R}^{N^3 \times N^2}$ satisfying $\mathbb{C}\mathbb{G} = 0$ and $\mathbb{D}\mathbb{C} = 0$. Their explicit form using tensor-products of univariate B-spline basis functions will be shown Section 3.4. Finally, we introduce the following symmetric mass matrices in each of the four discrete spaces which follow from the definitions of the L^2 -inner products (A.6):

$$\mathbb{M}^0 := \int_{\hat{\Omega}} \boldsymbol{\Lambda}^0 (\boldsymbol{\Lambda}^0)^\top \sqrt{g} \, d^3 \eta, \quad \in \mathbb{R}^{N^0 \times N^0}, \quad (3.7a)$$

$$\mathbb{M}^1 := \int_{\hat{\Omega}} \boldsymbol{\Lambda}^1 G^{-1} (\boldsymbol{\Lambda}^1)^\top \sqrt{g} \, d^3 \eta, \quad \in \mathbb{R}^{N^1 \times N^1}, \quad (3.7b)$$

$$\mathbb{M}^2 := \int_{\hat{\Omega}} \boldsymbol{\Lambda}^2 G (\boldsymbol{\Lambda}^2)^\top \frac{1}{\sqrt{g}} \, d^3 \eta, \quad \in \mathbb{R}^{N^2 \times N^2}, \quad (3.7c)$$

$$\mathbb{M}^3 := \int_{\hat{\Omega}} \boldsymbol{\Lambda}^3 (\boldsymbol{\Lambda}^3)^\top \frac{1}{\sqrt{g}} \, d^3 \eta, \quad \in \mathbb{R}^{N^3 \times N^3}. \quad (3.7d)$$

3.2 Strong equations: mass continuity and induction equation

As already indicated in Section 2.4, we keep the mass conservation law and induction equation in strong form to achieve point-wise conservation of mass and $\nabla \cdot \mathbf{B} = 0$. Hence we take (2.15a), project it on the space V_3 , make use of the commutativity relations (3.3), replace $\hat{\mathbf{U}}^1$ by its approximation $\hat{\mathbf{U}}_h^1$ and insert the expansions (3.5b) and (3.5d) in the respective basis:

$$\frac{\partial \hat{\rho}_h^3}{\partial t} + \hat{\nabla} \cdot \mathbf{\Pi}_2 \left[\hat{\rho}_{\text{eq}}^3 G^{-1} \hat{\mathbf{U}}_h^1 \right] = 0, \quad (3.8)$$

$$\Leftrightarrow (\mathbf{\Lambda}^3)^\top \frac{d\boldsymbol{\rho}}{dt} + (\mathbf{\Lambda}^3)^\top \mathbb{D} \tilde{\mathbf{\Pi}}_2 \left[\hat{\rho}_{\text{eq}}^3 G^{-1} (\mathbf{\Lambda}^1)^\top \right] \mathbf{u} = 0, \quad (3.9)$$

$$\Leftrightarrow \frac{d\boldsymbol{\rho}}{dt} + \mathbb{D} \mathcal{Q} \mathbf{u} = 0. \quad (3.10)$$

Moreover, in the last line, we introduced the projection matrix $\mathcal{Q} \in \mathbb{R}^{N^2 \times N^1}$ which can be seen as a matrix containing all coefficients in the space V_2 (lines) of all projected basis functions in V_1 weighted with some quantity (columns), here the equilibrium 3-form density $\hat{\rho}_{\text{eq}}^3$ multiplied by the inverse metric tensor G^{-1} . Explicitly,

$$\mathcal{Q} := \left(\tilde{\mathbf{\Pi}}_2 \left[\hat{\rho}_{\text{eq}}^3 G^{-1} \begin{pmatrix} \Lambda_{1,i}^1 \\ 0 \\ 0 \end{pmatrix} \right]_{0 \leq i < N_1^1}, \tilde{\mathbf{\Pi}}_2 \left[\hat{\rho}_{\text{eq}}^3 G^{-1} \begin{pmatrix} 0 \\ \Lambda_{2,i}^1 \\ 0 \end{pmatrix} \right]_{0 \leq i < N_2^1}, \tilde{\mathbf{\Pi}}_2 \left[\hat{\rho}_{\text{eq}}^3 G^{-1} \begin{pmatrix} 0 \\ 0 \\ \Lambda_{3,i}^1 \end{pmatrix} \right]_{0 \leq i < N_3^1} \right). \quad (3.11)$$

We place a tilde over the projectors, e.g. $\tilde{\mathbf{\Pi}}_3$, to indicate the restriction to the coefficients of a projection, excluding the basis functions, e.g. $\mathbf{\Pi}_3 \hat{\rho}^3 = \hat{\rho}_h^3 = (\mathbf{\Lambda}^3)^\top \boldsymbol{\rho} \in V_3$ but $\tilde{\mathbf{\Pi}}_3 \hat{\rho}^3 = \boldsymbol{\rho} \in \mathbb{R}^{N^3}$. According to (3.10), the discrete mass evolves in time as

$$\frac{d}{dt} \int_{\hat{\Omega}} \hat{\rho}_h^3 d^3 \eta = \left(\frac{d\boldsymbol{\rho}}{dt} \right)^\top \int_{\hat{\Omega}} \mathbf{\Lambda}^3 d^3 \eta = -\mathbf{u}^\top \mathcal{Q}^\top \mathbb{D}^\top \underbrace{\int_{\hat{\Omega}} \mathbf{\Lambda}^3 d^3 \eta}_{=(1,1,\dots,1,1)^\top} = 0, \quad (3.12)$$

since the basis functions in V_3 are all normalized to one in case of the B-spline construction shown in Section 3.4 and the corresponding discrete divergence matrix \mathbb{D} takes the difference of specific values of the vector it is applied to. Consequently, mass is conserved.

In the same way, we obtain for the induction equation (2.15d)

$$\frac{\partial \hat{\mathbf{B}}_h^2}{\partial t} + \hat{\nabla} \times \mathbf{\Pi}_1 \left[\mathbb{B}_{\text{eq}} G^{-1} \hat{\mathbf{U}}_h^1 \right] = 0, \quad (3.13)$$

$$\Leftrightarrow (\mathbf{\Lambda}^2)^\top \frac{d\mathbf{b}}{dt} + (\mathbf{\Lambda}^2)^\top \mathbb{C} \tilde{\mathbf{\Pi}}_1 \left[\mathbb{B}_{\text{eq}} G^{-1} (\mathbf{\Lambda}^1)^\top \right] \mathbf{u} = 0, \quad (3.14)$$

$$\Leftrightarrow \frac{d\mathbf{b}}{dt} + \mathbb{C} \mathcal{T} \mathbf{u} = 0, \quad (3.15)$$

where we wrote the cross product of the background magnetic field with another vector in terms of a matrix-vector product by using the anti-symmetric matrix

$$\mathbb{B}_{\text{eq}} := \begin{pmatrix} 0 & -\hat{B}_{\text{eq},3} & \hat{B}_{\text{eq},2} \\ \hat{B}_{\text{eq},3} & 0 & -\hat{B}_{\text{eq},1} \\ -\hat{B}_{\text{eq},2} & \hat{B}_{\text{eq},1} & 0 \end{pmatrix} \in \mathbb{R}^{3 \times 3}. \quad (3.16)$$

Moreover, we introduced another projection matrix $\mathcal{T} \in \mathbb{R}^{N^1 \times N^1}$:

$$\mathcal{T} := \left(\tilde{\mathbf{\Pi}}_1 \left[\mathbb{B}_{\text{eq}} G^{-1} \begin{pmatrix} \Lambda_{1,i}^1 \\ 0 \\ 0 \end{pmatrix} \right]_{0 \leq i < N_1^1}, \tilde{\mathbf{\Pi}}_1 \left[\mathbb{B}_{\text{eq}} G^{-1} \begin{pmatrix} 0 \\ \Lambda_{2,i}^1 \\ 0 \end{pmatrix} \right]_{0 \leq i < N_2^1}, \tilde{\mathbf{\Pi}}_1 \left[\mathbb{B}_{\text{eq}} G^{-1} \begin{pmatrix} 0 \\ 0 \\ \Lambda_{3,i}^1 \end{pmatrix} \right]_{0 \leq i < N_3^1} \right). \quad (3.17)$$

Finally, we note that (3.15) preserves the zero-divergence constraint for the magnetic field,

$$\frac{\partial}{\partial t}(\hat{\nabla} \cdot \hat{\mathbf{B}}_h^2) = \left(\mathbb{D} \frac{d\mathbf{b}}{dt} \right)^\top \boldsymbol{\Lambda}^3 = -(\mathbb{D}\mathcal{C}\mathcal{T}\mathbf{u})^\top \boldsymbol{\Lambda}^3 = 0, \quad (3.18)$$

due to $\mathbb{D}\mathcal{C} = 0$, a consequence of the special choice of compatible finite element spaces forming an exact de Rham sequence. The satisfaction of the zero-divergence constraint at $t = 0$ is ensured by the commuting diagram property:

$$\hat{\nabla} \cdot \hat{\mathbf{B}}_h^2(t=0) = \hat{\nabla} \cdot \boldsymbol{\Pi}_2 \hat{\mathbf{B}}^2(t=0) = \boldsymbol{\Pi}_3 \left[\hat{\nabla} \cdot \hat{\mathbf{B}}^2(t=0) \right] = 0. \quad (3.19)$$

An example will be shown in Section 3.4.

3.3 Weak equations: momentum balance and pressure equation

We choose a weak formulation for the momentum balance equation (2.15b). Consequently, we take the L^2 -inner product of 1-forms defined in (A.6) with a test function $\hat{\mathbf{C}}^1 \in H(\text{curl}, \hat{\Omega})$:

$$\begin{aligned} \int_{\hat{\Omega}} \frac{\hat{\rho}_{\text{eq}}^3}{\sqrt{g}} \left(\frac{\partial \hat{\mathbf{U}}^1}{\partial t} \right)^\top G^{-1} \hat{\mathbf{C}}^1 \sqrt{g} d^3\eta &= \int_{\hat{\Omega}} \left\{ \left[\hat{\nabla} \times \left(\frac{1}{\sqrt{g}} G \hat{\mathbf{B}}^2 \right) \right] \times \left(\frac{1}{\sqrt{g}} \hat{\mathbf{B}}_{\text{eq}}^2 \right) \right\}^\top G^{-1} \hat{\mathbf{C}}^1 \sqrt{g} d^3\eta \\ &+ \int_{\hat{\Omega}} \left\{ \left[\hat{\nabla} \times \left(\frac{1}{\sqrt{g}} G \hat{\mathbf{B}}_{\text{eq}}^2 \right) \right] \times \left(\frac{1}{\sqrt{g}} \hat{\mathbf{B}}^2 \right) \right\}^\top G^{-1} \hat{\mathbf{C}}^1 \sqrt{g} d^3\eta \\ &- \int_{\hat{\Omega}} (\hat{\nabla} \hat{p}^0)^\top G^{-1} \hat{\mathbf{C}}^1 \sqrt{g} d^3\eta \\ &- \underbrace{\int_{\hat{\Omega}} \frac{\hat{\rho}_{\text{f}}^3}{\sqrt{g}} \left(\hat{\mathbf{B}}_{\text{f}}^2 \times G^{-1} \hat{\mathbf{U}}^1 \right)^\top G^{-1} \hat{\mathbf{C}}^1 \sqrt{g} d^3\eta}_{:= \text{CC}(\rho_{\text{h}})} \\ &+ \underbrace{\int_{\hat{\Omega}} \frac{1}{\sqrt{g}} \left(\hat{\mathbf{B}}_{\text{f}}^2 \times \hat{\mathbf{J}}_{\text{h}}^2 \right)^\top G^{-1} \hat{\mathbf{C}}^1 \sqrt{g} d^3\eta}_{:= \text{CC}(\mathbf{J}_{\text{h}})} \quad \forall \hat{\mathbf{C}}^1 \in H(\text{curl}, \hat{\Omega}). \end{aligned} \quad (3.20)$$

The last two terms $\text{CC}(\rho_{\text{h}})$ and $\text{CC}(\mathbf{J}_{\text{h}})$, involving the coupling to the kinetic species via the charge density ρ_{h} and the current density \mathbf{J}_{h} , are treated separately in Section 3.5. From an energy conservation point of view, the inertia term on the left-hand side and the first Lorentz-force term on the right-hand side of (3.20) are in particular important. Regarding the latter, we use $\mathbf{a} \cdot (\mathbf{b} \times \mathbf{c}) = \mathbf{c} \cdot (\mathbf{a} \times \mathbf{b})$ and integrate by parts (assuming the boundary term vanishes) to obtain

$$\begin{aligned} \int_{\hat{\Omega}} \left\{ \left[\hat{\nabla} \times \left(\frac{1}{\sqrt{g}} G \hat{\mathbf{B}}^2 \right) \right] \times \left(\frac{1}{\sqrt{g}} \hat{\mathbf{B}}_{\text{eq}}^2 \right) \right\}^\top G^{-1} \hat{\mathbf{C}}^1 \sqrt{g} d^3\eta &= \\ &= \int_{\hat{\Omega}} \left(\frac{1}{\sqrt{g}} G \hat{\mathbf{B}}^2 \right)^\top \hat{\nabla} \times \left(\hat{\mathbf{B}}_{\text{eq}}^2 \times G^{-1} \hat{\mathbf{C}}^1 \right) d^3\eta. \end{aligned} \quad (3.21)$$

We recognize the symmetry to the induction equation (2.15d) if we set $\hat{\mathbf{C}}^1 = \hat{\mathbf{U}}^1$ and if the induction equation is tested with $\hat{\mathbf{B}}^2$ via the scalar product of 2-forms.

In order to obtain a discrete version of (3.20), we make use of the projectors $\boldsymbol{\Pi}_1$ and $\boldsymbol{\Pi}_2$ and approximate scalar products of 1-forms and 2-forms, respectively, by

$$(a^1, b^1) = \int_{\hat{\Omega}} (\hat{\mathbf{a}}^1)^\top G^{-1} \hat{\mathbf{b}}^1 \sqrt{g} d^3\eta \approx \int_{\hat{\Omega}} (\boldsymbol{\Pi}_1 \hat{\mathbf{a}}^1)^\top G^{-1} (\boldsymbol{\Pi}_1 \hat{\mathbf{b}}^1) \sqrt{g} d^3\eta, \quad (3.22)$$

$$(a^2, b^2) = \int_{\hat{\Omega}} (\hat{\mathbf{a}}^2)^\top G \hat{\mathbf{b}}^2 \frac{1}{\sqrt{g}} d^3\eta \approx \int_{\hat{\Omega}} (\boldsymbol{\Pi}_2 \hat{\mathbf{a}}^2)^\top G (\boldsymbol{\Pi}_2 \hat{\mathbf{b}}^2) \frac{1}{\sqrt{g}} d^3\eta. \quad (3.23)$$

For reasons of conservation of energy, we take the following average for the inertia term on the left-hand side of (3.20):

$$\begin{aligned} \int_{\hat{\Omega}} \frac{\hat{\rho}_{\text{eq}}^3}{\sqrt{g}} \left(\frac{\partial \hat{\mathbf{U}}^1}{\partial t} \right)^\top G^{-1} \hat{\mathbf{C}}^1 \sqrt{g} d^3 \eta &\approx \frac{1}{2} \int_{\hat{\Omega}} \left[\tilde{\mathbf{\Pi}}_1 \left(\frac{\hat{\rho}_{\text{eq}}^3}{\sqrt{g}} \frac{\partial \hat{\mathbf{U}}_h^1}{\partial t} \right) \right]^\top G^{-1} \hat{\mathbf{C}}_h^1 \sqrt{g} d^3 \eta \\ &+ \frac{1}{2} \int_{\hat{\Omega}} \left(\frac{\partial \hat{\mathbf{U}}^1}{\partial t} \right)^\top G^{-1} \tilde{\mathbf{\Pi}}_1 \left(\frac{\hat{\rho}_{\text{eq}}^3}{\sqrt{g}} \hat{\mathbf{C}}_h^1 \right) \sqrt{g} d^3 \eta. \end{aligned} \quad (3.24)$$

Expanding $\hat{\mathbf{U}}_h^1$ and $\hat{\mathbf{C}}_h^1$ in the basis of V_1 yields

$$\int_{\hat{\Omega}} \left(\frac{\partial \hat{\mathbf{U}}^1}{\partial t} \right)^\top G^{-1} \tilde{\mathbf{\Pi}}_1 \left(\frac{\hat{\rho}_{\text{eq}}^3}{\sqrt{g}} \hat{\mathbf{C}}_h^1 \right) \sqrt{g} d^3 \eta = \left(\frac{d\mathbf{u}}{dt} \right)^\top \underbrace{\int_{\hat{\Omega}} \Lambda^1 G^{-1} (\Lambda^1)^\top \sqrt{g} d^3 \eta}_{=\mathbb{M}^1} \tilde{\mathbf{\Pi}}_1 \left[\frac{\hat{\rho}_{\text{eq}}^3}{\sqrt{g}} (\Lambda^1)^\top \right] \mathbf{c}. \quad (3.25)$$

We recognize the mass matrix \mathbb{M}^1 and another projection matrix $\mathcal{W} \in \mathbb{R}^{N^1 \times N^1}$ defined as

$$\mathcal{W} := \left(\tilde{\mathbf{\Pi}}_1 \left[\frac{\hat{\rho}_{\text{eq}}^3}{\sqrt{g}} \begin{pmatrix} \Lambda_{1,i}^1 \\ 0 \\ 0 \end{pmatrix} \right]_{0 \leq i < N_1^1}, \tilde{\mathbf{\Pi}}_1 \left[\frac{\hat{\rho}_{\text{eq}}^3}{\sqrt{g}} \begin{pmatrix} 0 \\ \Lambda_{2,i}^1 \\ 0 \end{pmatrix} \right]_{0 \leq i < N_2^1}, \tilde{\mathbf{\Pi}}_1 \left[\frac{\hat{\rho}_{\text{eq}}^3}{\sqrt{g}} \begin{pmatrix} 0 \\ 0 \\ \Lambda_{3,i}^1 \end{pmatrix} \right]_{0 \leq i < N_3^1} \right). \quad (3.26)$$

Note that \mathcal{W} is the identity times a constant value if $\rho_{\text{eq}} = \hat{\rho}_{\text{eq}}^3 / \sqrt{g}$ is independent of $\boldsymbol{\eta}$. Finally, the inertia term is discretized as

$$\int_{\hat{\Omega}} \frac{\hat{\rho}_{\text{eq}}^3}{\sqrt{g}} \left(\frac{\partial \hat{\mathbf{U}}^1}{\partial t} \right)^\top G^{-1} \hat{\mathbf{C}}^1 \sqrt{g} d^3 \eta \approx \left(\frac{d\mathbf{u}}{dt} \right)^\top \frac{1}{2} (\mathcal{W}^\top \mathbb{M}^1 + \mathbb{M}^1 \mathcal{W}) \mathbf{c} =: \mathbf{c}^\top \mathcal{A} \frac{d\mathbf{u}}{dt}, \quad (3.27)$$

where $\mathcal{A} \in \mathbb{R}^{N^1 \times N^1}$ is symmetric. Using (3.23) and the commutativity of $\tilde{\mathbf{\Pi}}_2$ and $\hat{\nabla} \times$, the right-hand side of (3.21) amounts to

$$\begin{aligned} \int_{\hat{\Omega}} (\hat{\mathbf{B}}^2)^\top G \hat{\nabla} \times (\hat{\mathbf{B}}_{\text{eq}}^2 \times G^{-1} \hat{\mathbf{C}}^1) \frac{1}{\sqrt{g}} d^3 \eta &\approx \int_{\hat{\Omega}} (\hat{\mathbf{B}}_h^2)^\top G \hat{\nabla} \times \tilde{\mathbf{\Pi}}_1 (\hat{\mathbf{B}}_{\text{eq}}^2 \times G^{-1} \hat{\mathbf{C}}_h^1) \frac{1}{\sqrt{g}} d^3 \eta \\ &= \mathbf{b}^\top \underbrace{\int_{\hat{\Omega}} \Lambda^2 G (\Lambda^2)^\top \frac{1}{\sqrt{g}} d^3 \eta}_{=\mathbb{M}^2} \tilde{\mathbf{\Pi}}_1 \left[\mathbb{B}_{\text{eq}} G^{-1} (\Lambda^1)^\top \right] \mathbf{c} \\ &=: \mathbf{b}^\top \mathbb{M}^2 \mathcal{C} \mathcal{T} \mathbf{c}, \end{aligned} \quad (3.28)$$

where \mathcal{T} is the same projection matrix as in the semi-discrete induction equation (3.15). As the same techniques are applied for the remaining two terms not involving a coupling to the kinetic species, we skip the detailed derivation and just give the resulting discrete versions which read

$$\begin{aligned} \int_{\hat{\Omega}} \left\{ \left[\hat{\nabla} \times \left(\frac{1}{\sqrt{g}} G \hat{\mathbf{B}}_{\text{eq}}^2 \right) \right] \times \left(\frac{1}{\sqrt{g}} \hat{\mathbf{B}}^2 \right) \right\}^\top G^{-1} \hat{\mathbf{C}}^1 \sqrt{g} d^3 \eta \\ \approx \mathbf{b}^\top \left[\tilde{\mathbf{\Pi}}_1 \left(\frac{1}{\sqrt{g}} \mathbb{B}_{\text{eq}}^{\hat{\nabla} \times} (\Lambda^2)^\top \right) \right]^\top \int_{\hat{\Omega}} \Lambda^1 G^{-1} (\Lambda^1)^\top \sqrt{g} d^3 \eta \mathbf{c} \\ =: \mathbf{b}^\top \mathcal{P}^\top \mathbb{M}^1 \mathbf{c}, \end{aligned} \quad (3.29)$$

$$\int_{\hat{\Omega}} (\hat{\nabla} \hat{p}^0)^\top G^{-1} \hat{\mathbf{C}}^1 \sqrt{g} d^3 \eta \approx \mathbf{p}^\top \mathbb{G}^\top \mathbb{M}^1 \mathbf{c}, \quad (3.30)$$

where $\mathcal{P} \in \mathbb{R}^{N^1 \times N^2}$, given by

$$\mathcal{P} := \left(\tilde{\mathbf{\Pi}}_1 \left[\frac{1}{\sqrt{g}} \mathbb{B}_{\text{eq}}^{\hat{\nabla} \times} \begin{pmatrix} \Lambda_{1,i}^2 \\ 0 \\ 0 \end{pmatrix} \right]_{0 \leq i < N_1^2}, \tilde{\mathbf{\Pi}}_1 \left[\frac{1}{\sqrt{g}} \mathbb{B}_{\text{eq}}^{\hat{\nabla} \times} \begin{pmatrix} 0 \\ \Lambda_{2,i}^2 \\ 0 \end{pmatrix} \right]_{0 \leq i < N_2^2}, \tilde{\mathbf{\Pi}}_1 \left[\frac{1}{\sqrt{g}} \mathbb{B}_{\text{eq}}^{\hat{\nabla} \times} \begin{pmatrix} 0 \\ 0 \\ \Lambda_{3,i}^2 \end{pmatrix} \right]_{0 \leq i < N_3^2} \right). \quad (3.31)$$

The expression $\mathbb{B}_{\text{eq}}^{\hat{\nabla} \times}$ represents again the cross product in terms of a matrix vector-multiplication like (3.16) but this time built from the three components of $\hat{\nabla} \times (G\hat{\mathbf{B}}_{\text{eq}}^2/\sqrt{g})$. In summary, we end up with semi-discrete momentum balance equation

$$\mathbf{c}^\top \mathcal{A} \dot{\mathbf{u}} = \mathbf{c}^\top \mathcal{T}^\top \mathbb{C}^\top \mathbb{M}^2 \mathbf{b} + \mathbf{c}^\top \mathbb{M}^1 \mathcal{P} \mathbf{b} - \mathbf{c}^\top \mathbb{M}^1 \mathbb{G} \mathbf{p} - \text{CC}(\rho_h) + \text{CC}(\mathbf{J}_h) \quad \forall \mathbf{c} \in \mathbb{R}^{N^1}, \quad (3.32)$$

with $\text{CC}(\rho_h)$ and $\text{CC}(\mathbf{J}_h)$ given in Section 3.5.

We obtain the following weak formulation for the pressure equation (2.15c) by taking the 0-form scalar product from (A.6) with a test function \hat{r}^0 :

$$\int_{\hat{\Omega}} \frac{\partial \hat{p}^0}{\partial t} \hat{r}^0 \sqrt{g} \, d^3 \eta - \int_{\hat{\Omega}} \hat{p}_{\text{eq}}^0 (\hat{\mathbf{U}}^1)^\top G^{-1} \hat{\nabla} \hat{r}^0 \sqrt{g} \, d^3 \eta - (\gamma - 1) \int_{\hat{\Omega}} (\hat{\mathbf{U}}^1)^\top G^{-1} \hat{\nabla} (\hat{p}_{\text{eq}}^0 \hat{r}^0) \sqrt{g} \, d^3 \eta = 0 \quad (3.33)$$

$\forall \hat{r}^0 \in H^1(\hat{\Omega}).$

Here, we integrated by parts the two terms involving the divergence operator. This form is easier to handle from an implementation point of view since it requires less projections. The discrete versions of the three terms in (3.33) are given by

$$\begin{aligned} \int_{\hat{\Omega}} \frac{\partial \hat{p}^0}{\partial t} \hat{r}^0 \sqrt{g} \, d^3 \eta &\approx \left(\frac{d\mathbf{p}}{dt} \right)^\top \int_{\hat{\Omega}} \boldsymbol{\Lambda}^0 (\boldsymbol{\Lambda}^0)^\top \sqrt{g} \, d^3 \eta \mathbf{r} \\ &= \left(\frac{d\mathbf{p}}{dt} \right)^\top \mathbb{M}^0 \mathbf{r}, \end{aligned} \quad (3.34)$$

$$\begin{aligned} \int_{\hat{\Omega}} \hat{p}_{\text{eq}}^0 (\hat{\mathbf{U}}^1)^\top G^{-1} \hat{\nabla} \hat{r}^0 \sqrt{g} \, d^3 \eta &\approx \mathbf{u}^\top \left[\tilde{\boldsymbol{\Pi}}_1 \left(\hat{p}_{\text{eq}}^0 (\boldsymbol{\Lambda}^1)^\top \right) \right]^\top \int_{\hat{\Omega}} \boldsymbol{\Lambda}^1 G^{-1} (\boldsymbol{\Lambda}^1)^\top \sqrt{g} \, d^3 \eta \mathbb{G} \mathbf{r} \\ &=: \mathbf{u}^\top \mathcal{S}^\top \mathbb{M}^1 \mathbb{G} \mathbf{r}, \end{aligned} \quad (3.35)$$

$$\begin{aligned} \int_{\hat{\Omega}} (\hat{\mathbf{U}}^1)^\top G^{-1} \hat{\nabla} (\hat{p}_{\text{eq}}^0 \hat{r}^0) \sqrt{g} \, d^3 \eta &\approx \mathbf{u}^\top \int_{\hat{\Omega}} \boldsymbol{\Lambda}^1 G^{-1} (\boldsymbol{\Lambda}^1)^\top \sqrt{g} \, d^3 \eta \mathbb{G} \tilde{\boldsymbol{\Pi}}_0 \left[\hat{p}_{\text{eq}}^0 (\boldsymbol{\Lambda}^0)^\top \right] \mathbf{r} \\ &=: \mathbf{u}^\top \mathbb{M}^1 \mathbb{G} \mathcal{K} \mathbf{r}, \end{aligned} \quad (3.36)$$

with $\mathcal{S} \in \mathbb{R}^{N^1 \times N^1}$ and $\mathcal{K} \in \mathbb{R}^{N^0 \times N^0}$ defined as

$$\mathcal{S} := \left(\tilde{\boldsymbol{\Pi}}_1 \left[\hat{p}_{\text{eq}}^0 \begin{pmatrix} \Lambda_{1,i}^1 \\ 0 \\ 0 \end{pmatrix} \right]_{0 \leq i < N_1^1}, \tilde{\boldsymbol{\Pi}}_1 \left[\hat{p}_{\text{eq}}^0 \begin{pmatrix} 0 \\ \Lambda_{2,i}^1 \\ 0 \end{pmatrix} \right]_{0 \leq i < N_2^1}, \tilde{\boldsymbol{\Pi}}_1 \left[\hat{p}_{\text{eq}}^0 \begin{pmatrix} 0 \\ 0 \\ \Lambda_{3,i}^1 \end{pmatrix} \right]_{0 \leq i < N_3^1} \right), \quad (3.37)$$

$$\mathcal{K} := \left(\boldsymbol{\Pi}_0 \left[\hat{p}_{\text{eq}}^0 \Lambda_i^0 \right]_{0 \leq i < N^0} \right). \quad (3.38)$$

In summary, the semi-discrete pressure equation reads

$$\mathbb{M}^0 \frac{d\mathbf{p}}{dt} = \mathbb{G}^\top \mathbb{M}^1 \mathcal{S} \mathbf{u} + (\gamma - 1) \mathcal{K}^\top \mathbb{G}^\top \mathbb{M}^1 \mathbf{u}, \quad (3.39)$$

due to the fact that we want each term to be true for all $\mathbf{r} \in \mathbb{R}^{N^0}$.

3.4 Commuting diagram with B-splines and quasi-interpolation

3.4.1 B-splines and discrete derivatives

In this section, we review the construction of the finite element spaces and projectors shown in the diagram in Figure 1 using tensor-products of univariate B-splines. B-splines are piece-wise polynomials of degree p with a compact support. A univariate family of B-splines on the 1d logical domain $\hat{\Omega} = [0, 1]$ is fully determined by a non-decreasing sequence of points (or knots) on the real line which we collect in a vector $\hat{T} = \{\eta_i\}_{0 \leq i \leq n+2p}$ called the *knot vector*. If the knot vector contains at a point m repeated

knots, ones says that this knot has multiplicity m . The i -th B-spline \hat{N}_i^p of degree p is then recursively defined by

$$\hat{N}_i^p(\eta) := w_i^p(\eta)\hat{N}_i^{p-1}(\eta) + (1 - w_{i+1}^p(\eta))\hat{N}_{i+1}^{p-1}(\eta), \quad w_i^p(\eta) := \frac{\eta - \eta_i}{\eta_{i+p} - \eta_i}, \quad (3.40a)$$

$$\hat{N}_i^0(\eta) := \begin{cases} 1, & \eta \in [\eta_i, \eta_{i+1}), \\ 0 & \text{else.} \end{cases} \quad (3.40b)$$

We note some important properties of a B-spline basis:

- B-splines are piece-wise polynomials of degree p ,
- B-splines are non-negative,
- Compact support: the support of \hat{N}_i^p is contained in $[\eta_i, \dots, \eta_{i+p+1})$,
- Partition of unity: $\sum_i \hat{N}_i^p(\eta) = 1, \forall \eta \in [0, 1]$,
- Local linear independence,
- If a knot η_i has multiplicity m then $\hat{N}_i^p \in C^{p-m}$ at η_i .

In this work, we shall consider two types of knot vectors yielding either a uniform, *clamped* basis or a uniform, periodic basis. The knot vectors are constructed from a uniform partition of the domain $\hat{\Omega} = [0, 1]$ into n elements of equal length h and certain extensions at the boundaries to obtain the two different types:

$$\text{clamped : } \hat{T} = \underbrace{\{0, \dots, 0\}}_{p \text{ times}}, \underbrace{\{0, h, 2h, \dots, 1 - 2h, 1 - h, 1, 1, \dots, 1\}}_{n+1 \text{ element boundaries}}, \underbrace{\{1, \dots, 1\}}_{p \text{ times}}, \quad (3.41)$$

$$\text{periodic : } \hat{T} = \underbrace{\{-ph, \dots, -h\}}_{p \text{ terms}}, \underbrace{\{0, h, 2h, \dots, 1 - 2h, 1 - h, 1, 1 + h, \dots, 1 + ph\}}_{n+1 \text{ element boundaries}}, \underbrace{\{1 + h, \dots, 1 + ph\}}_{p \text{ terms}}. \quad (3.42)$$

The former knot vector is chosen such that the basis becomes interpolatory at the domain boundaries to facilitate the application of Dirichlet boundary conditions:

$$\hat{N}_0^p(0) = 1, \quad \hat{N}_i^p(0) = 0 \quad \forall i \in \{1, \dots, n + p - 1\}, \quad (3.43)$$

$$\hat{N}_{n+p-1}^p(1) = 1, \quad \hat{N}_i^p(1) = 0 \quad \forall i \in \{0, \dots, n + p - 2\}. \quad (3.44)$$

Another property which is in particular import for the construction of the discrete finite element spaces is that the derivative of a B-spline is given by

$$\frac{d\hat{N}_i^p}{d\eta} = \frac{p}{\eta_{i+p} - \eta_i} \hat{N}_i^{p-1} - \frac{p}{\eta_{i+p+1} - \eta_{i+1}} \hat{N}_{i+1}^{p-1} := \hat{D}_{i-1}^{p-1} - \hat{D}_i^{p-1}, \quad (3.45)$$

where we defined scaled splines of one degree less which we call *D-splines*⁴ and which are normalized to one. Note that $\hat{D}_{-1}^{p-1} = \hat{D}_{n+p-1}^{p-1} = 0$ which is why we remove these two splines from the space of D-splines. Furthermore, in case of periodic splines, we relate the last p (resp. $p - 1$ in case of the D-splines) splines to the first p (resp. $p - 1$) splines to ensure periodicity. Hence the number of *distinct* B-splines and D-splines, denoted by \hat{n}_N and \hat{n}_D , respectively, reduces to

$$\text{clamped : } \hat{n}_N = n + p \quad \hat{n}_D = \hat{n}_N - 1, \quad (3.46)$$

$$\text{periodic : } \hat{n}_N = n \quad \hat{n}_D = \hat{n}_N. \quad (3.47)$$

⁴It is convenient to start the indexing of the D-splines with -1 instead of 0.

the block matrices

$$\mathbb{G} := \begin{pmatrix} \hat{\mathbb{G}}^1 \otimes \mathbb{I}_{\hat{n}_N^2} \otimes \mathbb{I}_{\hat{n}_N^3} \\ \mathbb{I}_{\hat{n}_N^1} \otimes \hat{\mathbb{G}}^2 \otimes \mathbb{I}_{\hat{n}_N^3} \\ \mathbb{I}_{\hat{n}_N^1} \otimes \mathbb{I}_{\hat{n}_N^2} \otimes \hat{\mathbb{G}}^3 \end{pmatrix}, \quad (3.52a)$$

$$\mathbb{C} := \begin{pmatrix} 0 & -\mathbb{I}_{\hat{n}_N^1} \otimes \mathbb{I}_{\hat{n}_D^2} \otimes \hat{\mathbb{G}}^3 & \mathbb{I}_{\hat{n}_N^1} \otimes \hat{\mathbb{G}}^2 \otimes \mathbb{I}_{\hat{n}_D^3} \\ \mathbb{I}_{\hat{n}_D^1} \otimes \mathbb{I}_{\hat{n}_N^2} \otimes \hat{\mathbb{G}}^3 & 0 & -\hat{\mathbb{G}}^1 \otimes \mathbb{I}_{\hat{n}_N^2} \otimes \mathbb{I}_{\hat{n}_D^3} \\ -\mathbb{I}_{\hat{n}_D^1} \otimes \hat{\mathbb{G}}^2 \otimes \mathbb{I}_{\hat{n}_N^3} & \hat{\mathbb{G}}^1 \otimes \mathbb{I}_{\hat{n}_D^2} \otimes \mathbb{I}_{\hat{n}_N^3} & 0 \end{pmatrix}, \quad (3.52b)$$

$$\mathbb{D} := \begin{pmatrix} \hat{\mathbb{G}}^1 \otimes \mathbb{I}_{\hat{n}_D^2} \otimes \mathbb{I}_{\hat{n}_D^3} & \mathbb{I}_{\hat{n}_D^1} \otimes \hat{\mathbb{G}}^2 \otimes \mathbb{I}_{\hat{n}_D^3} & \mathbb{I}_{\hat{n}_D^1} \otimes \mathbb{I}_{\hat{n}_D^2} \otimes \hat{\mathbb{G}}^3 \end{pmatrix}. \quad (3.52c)$$

It can easily be verified that $\mathbb{C}\mathbb{G} = 0$ and $\mathbb{D}\mathbb{C} = 0$.

3.4.2 Commuting projectors

To ensure the commutativity of the diagram shown in Figure 1, we start from a one-dimensional quasi-interpolation method denoted by I^p onto the family of univariate B-splines of degree p defined by (3.40) and construct the corresponding commuting projector H^{p-1} according to

$$H^{p-1}f := \frac{d}{d\eta} I^p \left[\eta \mapsto \int_{\tau}^{\eta} f(t) dt \right], \quad (3.53)$$

for some continuous function $f \in C([0,1])$. It is easily verified that $d(I^p f)/d\eta = H^{p-1}(df/d\eta)$. The lower integration boundary τ can be chosen arbitrarily. The 3d projection operators are then constructed similarly to the basis functions (3.51) and discrete derivatives (3.52) by tensor-product considerations from the 1d operators. Note that the method explained hereafter is a rather special case of more general quasi spline interpolation techniques with the following properties [13]:

1. $I^p f$ is *local* in the sense that the value of $I^p f$ at η depends only on the values of f in a somewhat close vicinity to η .
2. I^p reproduces B-splines: $I^p \hat{N}_i^p = \hat{N}_i^p \quad \forall i$.
3. $|I^p f - f| = \mathcal{O}(|h|^{p+1})$.

The motivation for our choice is in particular the locality of the method (first point) since this has the consequence that all matrices involving projections (e.g. (3.11)) are sparse which would not be the case if we chose a global interpolation method.

Given a knot vector $\hat{T} = \{\eta_i\}_{0 \leq i \leq n+2p}$, we perform the following steps to obtain the i -th coefficient $\lambda_i(f)$ of the quasi-interpolant

$$I^p f = \sum_{i=0}^{\hat{n}_N-1} \lambda_i(f) \hat{N}_i^p : \quad (3.54)$$

1. Choose $2p - 1$ equidistant interpolation points $\{x_j^i\}_{0 \leq j < 2p-1}$ in the sub-interval $Q = [\eta_{\mu}, \eta_{\nu}]$ given by

$$\text{clamped : } Q := \begin{cases} [\eta_p, \eta_{2p-1}], & i < p - 1, \\ [\eta_{i+1}, \eta_{i+p}], & p - 1 \leq i \leq \hat{n}_N - p, \\ [\eta_{\hat{n}_N-p+1}, \eta_{\hat{n}_N}], & i > \hat{n}_N - p, \end{cases} \quad (3.55)$$

$$\text{periodic : } Q := [\eta_{i+1}, \eta_{i+p}], \quad \forall i. \quad (3.56)$$

2. Construct a local interpolant $I^Q f$ by solving the linear system

$$I^Q f(x_j^i) := \sum_{k=\mu-p}^{\nu-1} f_k \hat{N}_k^p(x_j^i) = f(x_j^i) \quad \forall j \in \{0, \dots, 2p-2\}. \quad (3.57)$$

3. Set $\lambda_i(f) = f_i$.

Solving (3.57) means that the i -th global coefficient can be written as a linear combination of function values at the interpolation points

$$\lambda_i(f) = \sum_{j=0}^{2p-2} \omega_j^i f(x_j^i), \quad (3.58)$$

where the weights $\omega^i = \{\omega_j^i\}_{0 \leq j < 2p-1}$ form the line of the inverse collocation matrix with entries $\hat{N}_k^p(x_j^i)$ corresponding the coefficient f_i . The resulting weights are shown in Table 3 in Appendix C for generic quadratic and cubic B-splines. In practice, we store the weights and use (3.58) to compute the coefficients of the quasi-interpolant (3.54).

Using (3.53), the corresponding commuting projector $H^{p-1}f$ can be derived in the following way:

$$\begin{aligned} H^{p-1}f &= \frac{d}{d\eta} \left[\sum_i \lambda_i \left(\eta \mapsto \int_{\tau}^{\eta} f(t) dt \right) \hat{N}_i^p \right] \\ &= - \sum_{i,j} \omega_j^i \int_{x_j^i}^{\tau} f(t) dt \frac{d\hat{N}_i^p}{d\eta} \\ &= \sum_i \left[\sum_j \left(\omega_j^i \int_{x_j^i}^{\tau} f(t) dt - \omega_{j+1}^i \int_{x_{j+1}^i}^{\tau} f(t) dt \right) \right] \hat{D}_i^{p-1} \\ &=: \sum_i \tilde{\lambda}_i(f) \hat{D}_i^{p-1} \end{aligned} \quad (3.59)$$

From the second to the third line we used the fact that the derivative of a B-spline is equal to the difference of two neighboring D-splines (in the same way as in (3.49)). If we define $2p + 1$ integration boundaries

$$\text{clamped : } \tilde{x}^i := \begin{cases} x^{p-1} \cup x^p, & i < p-1, \\ x^i \cup x^{i+1}, & p-1 \leq i \leq \hat{n}_D - p, \\ x^{\hat{n}_D - p} \cup x^{\hat{n}_D - p + 1}, & i > \hat{n}_D - p, \end{cases} \quad (3.60)$$

$$\text{periodic : } \tilde{x}^i := x^i \cup x^{i+1}, \quad \forall i, \quad (3.61)$$

set $\tau = x_{2p-2}^{i+1}$ and split the integrals into integrals between two neighboring interpolation points, it is straightforward to show that the i -th coefficient can be computed as

$$\tilde{\lambda}_i(f) = \sum_{j=0}^{2p-1} \tilde{\omega}_j^i \int_{\tilde{x}_j^i}^{\tilde{x}_{j+1}^i} f(t) dt, \quad (3.62)$$

with new weights given in Table 4 once more for generic degrees two and three⁶. In practice, we compute the integrals using $n_{\text{q,pr}} > p$ Gauss-Legendre quadrature points and weights per integration interval $[\tilde{x}_j^i, \tilde{x}_{j+1}^i]$.

The three-dimensional projectors Π_0 , Π_1 , Π_2 and Π_3 can now be constructed via compositions of the 1d operators I^p and H^{p-1} , respectively:

$$\Pi_0 = I^{p_1} \odot I^{p_2} \odot I^{p_3} \quad := \quad I^{p_1}(\eta_1 \mapsto I^{p_2}(\eta_2 \mapsto I^{p_3}(\eta_3 \mapsto f(\eta_1, \eta_2, \eta_3)))), \quad (3.63a)$$

$$\Pi_1 = \begin{pmatrix} H^{p_1-1} \odot I^{p_2} \odot I^{p_3} \\ I^{p_1} \odot H^{p_2-1} \odot I^{p_3} \\ I^{p_1} \odot I^{p_2} \odot H^{p_3-1} \end{pmatrix}, \quad (3.63b)$$

$$\Pi_2 = \begin{pmatrix} I^{p_1} \odot H^{p_2-1} \odot H^{p_3-1} \\ H^{p_1-1} \odot I^{p_2} \odot H^{p_3-1} \\ H^{p_1-1} \odot H^{p_2-1} \odot I^{p_3} \end{pmatrix}, \quad (3.63c)$$

$$\Pi_3 = H^{p_1-1} \odot H^{p_2-1} \odot H^{p_3-1}. \quad (3.63d)$$

⁶Note that we always refer to the degree of the B-splines. Of course, if e.g. $p = 3$, we have quadratic D-splines.

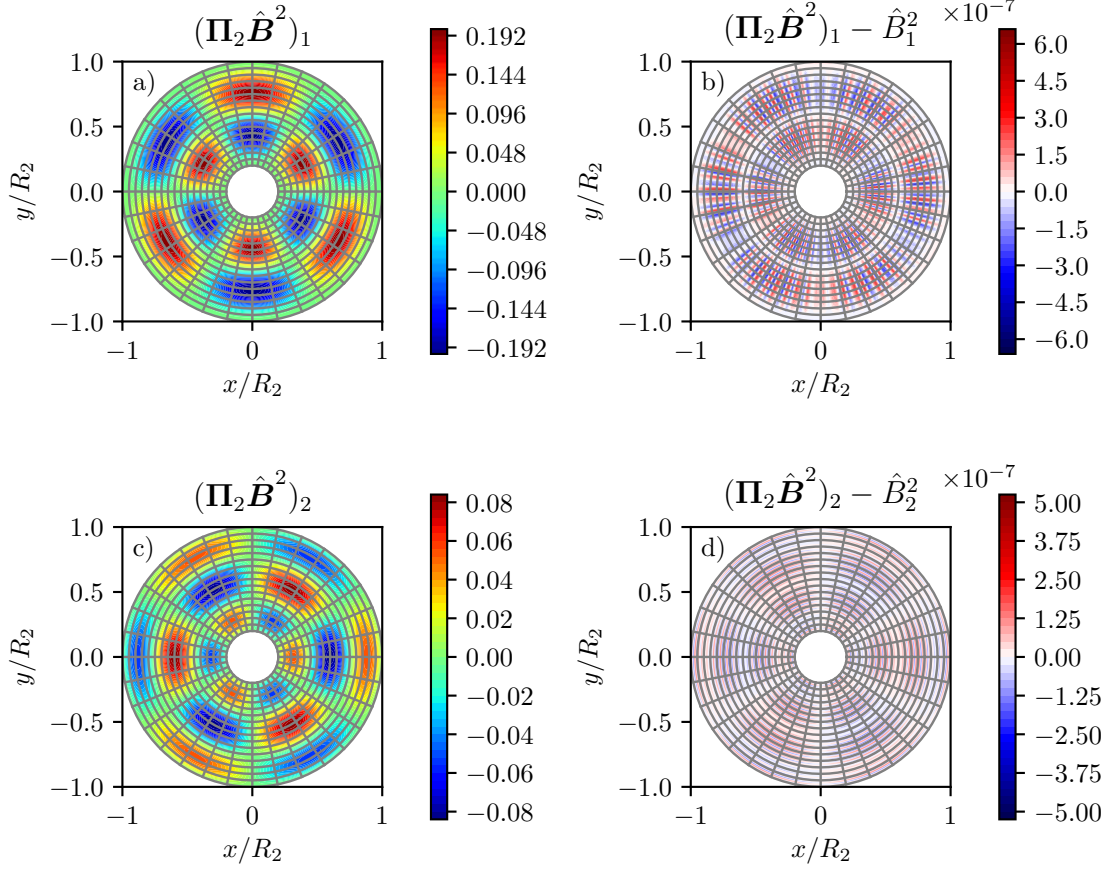


Figure 2: Projection of the 2-form components (3.65) using the projector (3.63c) on an annulus defined by the mapping (3.64) obtained with B-splines of degree $p = (3, 3, 1)$. The number of elements $N_{\text{el}} = (128, 256, 2)$, number of quadrature points per integration interval $n_{\text{q,pr}} = (6, 6, 2)$ and number of quadrature points per element for the computation of (3.66) $n_{\text{q,el}} = (6, 6, 2)$. a) Contour plots at $z = 0.5L_z$ of the numerical 1-component and b) corresponding error. c) Contour plots at $z = 0.5L_z$ of the numerical 2-component and d) corresponding error.

As an example, we project the components of a given 2-form $\hat{\mathbf{B}}^2$ satisfying $\hat{\nabla} \cdot \hat{\mathbf{B}}^2 = 0$ on an annulus in the xy -plane with inner radius R_1 and outer radius R_2 , such that $\Delta R = R_2 - R_1$. For completeness, we prescribe an extent of length L_z in z -direction. This geometry can be described by the mapping

$$\mathbf{F} : \hat{\Omega} \rightarrow \Omega, \quad \boldsymbol{\eta} \mapsto \begin{pmatrix} (R_1 + \eta_1 \Delta R) \cos(2\pi\eta_2) \\ (R_1 + \eta_1 \Delta R) \sin(2\pi\eta_2) \\ L_z \eta_3 \end{pmatrix} = \begin{pmatrix} x \\ y \\ z \end{pmatrix}. \quad (3.64)$$

We choose the components

$$\hat{\mathbf{B}}^2(\boldsymbol{\eta}) = \begin{pmatrix} \eta_1(1 - \eta_1) \sin(2\pi\eta_1) \sin(6\pi\eta_2) \\ \frac{1}{6\pi}(1 - 2\eta_1) \sin(2\pi\eta_1) + \eta_1(1 - \eta_1) \cos(2\pi\eta_1) 2\pi \cos(6\pi\eta_2) \\ 0 \end{pmatrix}, \quad (3.65)$$

clamped B-splines for the radial-like coordinate η_1 and periodic B-splines for the angle-like coordinate η_2 as well as for the third coordinate η_3 . We measure the error of the projected components compared to the exact ones in the L^2 -norm of the space of 2-forms,

$$\|\Delta \hat{\mathbf{B}}^2\|_{L^2} := \|\hat{\mathbf{B}}^2 - \Pi_2 \hat{\mathbf{B}}^2\|_{L^2} = \int_{\hat{\Omega}} (\hat{\mathbf{B}}^2 - \Pi_2 \hat{\mathbf{B}}^2)^\top G (\hat{\mathbf{B}}^2 - \Pi_2 \hat{\mathbf{B}}^2) \frac{1}{\sqrt{g}} d^3\boldsymbol{\eta}, \quad (3.66)$$

as we refine the mesh (that is, as we increase the number of elements), computed using $n_{\text{q,el}} = (6, 6, 2)$ Gauss-Legendre quadrature points per element on the logical domain. Furthermore, to verify the

commuting diagram property, we estimate the spatial L^∞ -norm of $\hat{\nabla} \cdot \Pi_2 \hat{\mathbf{B}}^2$,

$$\|\hat{\nabla} \cdot \Pi_2 \hat{\mathbf{B}}^2\|_{L^\infty} := \max_{(\eta_1, \eta_2, \eta_3) \in \hat{\Omega}} |\hat{\nabla} \cdot \Pi_2 \hat{\mathbf{B}}^2|, \quad (3.67)$$

at the Greville points [15]. The resulting projected components are shown in Figure 2 for typical parameters. Table 1 shows the convergence of the projector while increasing the number of elements using quadratic and cubic splines. It can be seen that the divergence of the projected field is close to zero ($\approx 10^{-13}$) for any spline degree and resolution. This shows that the commuting diagram property is satisfied exactly. Moreover, we remark that the exactness of the divergence-free projected field for arbitrary mesh resolution relies on the number of quadrature points used in the computation of the integrals in (3.62). Here, we used $n_{\text{q,pr}} = (6, 6, 2)$ Gauss-Legendre quadrature points per integration interval. Using $n_{\text{q,pr}} = (3, 3, 2)$ instead yields for quadratic splines ($p = (2, 2, 1)$) and $N_{\text{el}} = (32, 64, 2)$ an error of $\approx 10^{-12}$ showing that one should keep in mind the number of quadrature points if one reduces the mesh resolution.

	$p = (2, 2, 1)$			$p = (3, 3, 1)$		
N_{el}	$\ \Delta \hat{\mathbf{B}}^2\ _{L^2}$	Order	$\ \hat{\nabla} \cdot \Pi_2 \hat{\mathbf{B}}^2\ _{L^\infty}$	$\ \Delta \hat{\mathbf{B}}^2\ _{L^2}$	Order	$\ \hat{\nabla} \cdot \Pi_2 \hat{\mathbf{B}}^2\ _{L^\infty}$
(32, 64, 2)	$2.75 \cdot 10^{-4}$		$1.50 \cdot 10^{-14}$	$1.50 \cdot 10^{-5}$		$3.05 \cdot 10^{-14}$
(64, 128, 2)	$6.81 \cdot 10^{-5}$	2.01	$2.90 \cdot 10^{-14}$	$1.56 \cdot 10^{-6}$	3.27	$5.62 \cdot 10^{-14}$
(128, 256, 2)	$1.70 \cdot 10^{-5}$	2.00	$5.08 \cdot 10^{-14}$	$1.82 \cdot 10^{-7}$	3.10	$8.13 \cdot 10^{-14}$
(256, 512, 2)	$4.25 \cdot 10^{-6}$	2.00	$1.54 \cdot 10^{-13}$	$2.21 \cdot 10^{-8}$	3.04	$2.74 \cdot 10^{-13}$
(512, 1024, 2)	$1.06 \cdot 10^{-6}$	2.00	$3.42 \cdot 10^{-13}$	$2.73 \cdot 10^{-9}$	3.02	$5.86 \cdot 10^{-13}$

Table 1: Projection of the components (3.65) using the projector (3.63c) on an annulus defined by the mapping (3.64): p -th order convergence of the projector and divergence close to machine precision.

3.5 PIC coupling terms

We solve the Vlasov equation (2.6b) with classical particle-in-cell techniques. Hence we assume a particle-like distribution function which, in physical space Ω , takes the form

$$f_{\text{h}} = f_{\text{h}}(t, \mathbf{x}, \mathbf{v}) \approx \sum_{k=1}^K w_k \delta(\mathbf{x} - \mathbf{x}_k(t)) \delta(\mathbf{v} - \mathbf{v}_k(t)), \quad (3.68)$$

where K is the total number of simulation markers (to which we simply refer to as particles), w_k is the weight of the k -th particle and $\mathbf{x}_k = \mathbf{x}_k(t)$ and $\mathbf{v}_k = \mathbf{v}_k(t)$ its position in phase space at time t satisfying the equations of motion

$$\frac{d\mathbf{x}_k}{dt} = \mathbf{v}_k, \quad \mathbf{x}_k(t=0) = \mathbf{x}_k^0, \quad (3.69a)$$

$$\frac{d\mathbf{v}_k}{dt} = \mathbf{B}(\mathbf{x}_k) \times \tilde{\mathbf{U}}(\mathbf{x}_k) + \mathbf{v}_k \times \mathbf{B}(\mathbf{x}_k), \quad \mathbf{v}_k(t=0) = \mathbf{v}_k^0. \quad (3.69b)$$

To transform the equations of motion (3.69) to logical spatial coordinates $\boldsymbol{\eta}_k$, we note that $d\mathbf{x}(\boldsymbol{\eta}(t))/dt = DF d\boldsymbol{\eta}/dt$ for the first equation. Regarding the second equation, we first write it in curvilinear coordinates ($\mathbf{B} = DF \hat{\mathbf{B}}_{\text{f}}$ and $\tilde{\mathbf{U}} = DF \hat{\mathbf{U}}$) and then use the relations (2.13) to transform the components $\hat{\mathbf{B}}_{\text{f}}$ and $\hat{\mathbf{U}}$ the corresponding 2-form and 1-form components, respectively. Finally, we replace the continuous forms by their finite element approximations to obtain

$$\frac{d\boldsymbol{\eta}_k}{dt} = DF^{-1}(\boldsymbol{\eta}_k) \mathbf{v}_k, \quad (3.70a)$$

$$\frac{d\mathbf{v}_k}{dt} = (DF^{-1}(\boldsymbol{\eta}_k))^\top \left[\hat{\mathbf{B}}_{\text{fh}}^2(\boldsymbol{\eta}_k) \times G^{-1}(\boldsymbol{\eta}_k) \hat{\mathbf{U}}_h^1(\boldsymbol{\eta}_k) - \hat{\mathbf{B}}_{\text{fh}}^2(\boldsymbol{\eta}_k) \times DF^{-1}(\boldsymbol{\eta}_k) \mathbf{v}_k \right]. \quad (3.70b)$$

Here, we once more used the identity $M\mathbf{b} \times M\mathbf{c} = \det(M)(M^{-1})^\top(\mathbf{b} \times \mathbf{c})$.

We now turn our attention to the two terms $\text{CC}(\rho_h)$ and $\text{CC}(\mathbf{J}_h)$ in the weak momentum balance equation (3.20) involving the hot charge and current density. Following classical PIC techniques, the resulting integrals are evaluated by Monte-Carlo estimates using the particle positions in phase space [4]. Explicitly,

$$\text{CC}(\rho_h) \approx \int_{\hat{\Omega}} (\hat{\mathbf{C}}_h^1)^\top G^{-1} \hat{\rho}_h \left(\hat{\mathbf{B}}_{fh}^2 \times G^{-1} \hat{\mathbf{U}}_h^1 \right) \sqrt{g} d^3 \eta \quad (3.71)$$

$$= \int_{\hat{\Omega}} \int_{\mathbb{R}^3} \left\{ (\hat{\mathbf{C}}_h^1)^\top G^{-1} \frac{\hat{f}_h}{\hat{s}_h} \left(\hat{\mathbf{B}}_{fh}^2 \times G^{-1} \hat{\mathbf{U}}_h^1 \right) \right\} \hat{s}_h \sqrt{g} d^3 v d^3 \eta \quad (3.72)$$

$$\approx \sum_{k=1}^K \frac{1}{K} \underbrace{\frac{\hat{f}_h^0(\boldsymbol{\eta}_k^0, \mathbf{v}_k^0)}{\hat{s}_h^0(\boldsymbol{\eta}_k^0, \mathbf{v}_k^0)}}_{=: w_k} (\hat{\mathbf{C}}_h^1)^\top(\boldsymbol{\eta}_k) G^{-1}(\boldsymbol{\eta}_k) \left(\hat{\mathbf{B}}_{fh}^2(\boldsymbol{\eta}_k) \times G^{-1}(\boldsymbol{\eta}_k) \hat{\mathbf{U}}_h^1(\boldsymbol{\eta}_k) \right), \quad (3.73)$$

where we introduced the probability density function (PDF) $\hat{s}_h = \hat{s}_h(t, \boldsymbol{\eta}, \mathbf{v}) = s_h(t, \mathbf{F}(\boldsymbol{\eta}), \mathbf{v})$, which must be normalized to one and from which we demand to satisfy the Vlasov equation. Regarding the former, it is important to note that

$$1 = \int_{\Omega} \int_{\mathbb{R}^3} s_h(t, \mathbf{x}, \mathbf{v}) d^3 v d^3 x = \int_{\hat{\Omega}} \int_{\mathbb{R}^3} \hat{s}_h(t, \boldsymbol{\eta}, \mathbf{v}) \sqrt{g}(\boldsymbol{\eta}) d^3 v d^3 \eta \quad \forall t \in \mathbb{R}_0^+, \quad (3.74)$$

such that the transformed PDF is given by $\tilde{s}_h := \hat{s}_h \sqrt{g}$. Then (3.72) can be interpreted as the expectation value of the random variable inside the curly brackets distributed under the PDF \tilde{s}_h with (3.73) being its estimator using the particle positions $(\boldsymbol{\eta}_k, \mathbf{v}_k)_{1 \leq k \leq N_p}$ in phase space. Finally, we made use of the fact that \hat{f}_h and \hat{s}_h are constant along a particle trajectory according to the Vlasov equation, that is, $d\hat{f}_h/dt = 0$ in a Lagrangian frame, i.e. $\hat{f}_h(t, \boldsymbol{\eta}_k(t), \mathbf{v}_k(t)) = \hat{f}_h^0(\boldsymbol{\eta}_k^0, \mathbf{v}_k^0)$, where $\hat{f}_h^0 = \hat{f}_h(t=0, \boldsymbol{\eta}, \mathbf{v}) = f_h(t=0, \mathbf{F}(\boldsymbol{\eta}), \mathbf{v})$ denotes the initial distribution function and $(\boldsymbol{\eta}_k^0, \mathbf{v}_k^0)$ is the initial position of the k -th particle in phase space drawn from the initial PDF \hat{s}_h^0 . Hence the particle weights $(w_k)_{1 \leq k \leq N_p}$ are constant in time which is not the case if, as shown in Appendix B, a δf approach is used. One should keep in mind that if one samples from the transformed PDF \tilde{s}_h , one must not forget the Jacobian determinant in the definition of the weights.

In order to write (3.73) as well as (3.70) in matrix-vector form, we introduce the following vectors and matrices:

- $\mathbf{H} \quad := (\eta_{1,1}, \dots, \eta_{K,1}, \eta_{1,2}, \dots, \eta_{K,2}, \eta_{1,3}, \dots, \eta_{K,3})^\top \in \mathbb{R}^{3K}$,
- $\mathbf{V} \quad := (v_{1,x}, \dots, v_{K,x}, v_{1,y}, \dots, v_{K,y}, v_{1,z}, \dots, v_{K,z})^\top \in \mathbb{R}^{3K}$,
- $\mathbb{W} \quad := \mathbb{I}_3 \otimes \text{diag}(w_1, \dots, w_K) \in \mathbb{R}^{3K \times 3K}$,
- $\mathbb{P}_\mu^n(\mathbf{H}) \quad := (\Lambda_{\mu,i}^n(\boldsymbol{\eta}_k))_{0 \leq i < N_\mu^n, 1 \leq k \leq K} \quad (n \in \{1, 2\}, \mu \in \{1, 2, 3\}) \in \mathbb{R}^{N_\mu^n \times K}$,
- $\mathbb{P}^n(\mathbf{H}) \quad := \text{diag}(\mathbb{P}_1^n, \mathbb{P}_2^n, \mathbb{P}_3^n) \quad (n \in \{1, 2\}) \in \mathbb{R}^{N^n \times 3K}$,
- $\bar{G}_{ab}^{-1}(\mathbf{H}) \quad := \text{diag}(G_{ab}^{-1}(\boldsymbol{\eta}_1), \dots, G_{ab}^{-1}(\boldsymbol{\eta}_K)) \quad (a, b \in \{1, 2, 3\}) \in \mathbb{R}^{K \times K}$,
- $\bar{G}^{-1}(\mathbf{H}) \quad := (\bar{G}_{ab}^{-1})_{1 \leq a, b \leq 3} \in \mathbb{R}^{3K \times 3K}$,
- $\bar{D}F_{ab}^{-1}(\mathbf{H}) \quad := \text{diag}(DF_{ab}^{-1}(\boldsymbol{\eta}_1), \dots, DF_{ab}^{-1}(\boldsymbol{\eta}_K)) \quad (a, b \in \{1, 2, 3\}) \in \mathbb{R}^{K \times K}$,
- $\bar{D}F^{-1}(\mathbf{H}) \quad := (\bar{D}F_{ab}^{-1})_{1 \leq a, b \leq 3} \in \mathbb{R}^{3K \times 3K}$,
- $\mathbb{B}_{f,\mu}(\mathbf{b}, \mathbf{H}) \quad := \text{diag}(\mathbf{b}_\mu^\top \mathbb{P}_\mu^2) + \text{diag}(\hat{B}_{\text{eq},\mu}(\boldsymbol{\eta}_1), \dots, \hat{B}_{\text{eq},\mu}(\boldsymbol{\eta}_K)) \quad \mu \in \{1, 2, 3\} \in \mathbb{R}^{K \times K}$,

where $\mathbb{I}_3 \in \mathbb{R}^{3 \times 3}$ denotes the 3×3 identity matrix and \otimes the Kronecker product. In accordance with (3.16), we additionally define the block matrix

$$\mathbb{B}_f = \mathbb{B}_f(\mathbf{b}, \mathbf{H}) := \begin{pmatrix} 0 & -\mathbb{B}_{f,3} & \mathbb{B}_{f,2} \\ \mathbb{B}_{f,3} & 0 & -\mathbb{B}_{f,1} \\ -\mathbb{B}_{f,2} & \mathbb{B}_{f,1} & 0 \end{pmatrix} \in \mathbb{R}^{3K \times 3K}, \quad (3.75)$$

which represents the cross product with the total magnetic field at all particle positions. With this (3.73) becomes

$$\text{CC}(\rho_h) \approx \mathbf{c}^\top \mathbb{P}^1 \mathbb{W} \bar{G}^{-1} \mathbb{B}_f \bar{G}^{-1} (\mathbb{P}^1)^\top \mathbf{u}. \quad (3.76)$$

The same procedure holds for the term involving the hot current density:

$$\text{CC}(\mathbf{J}_h) \approx \int_{\hat{\Omega}} (\hat{\mathbf{C}}_h^1)^\top G^{-1} \left(\hat{\mathbf{B}}_{fh}^2 \times \hat{\mathbf{J}}_h \right) \sqrt{g} d^3 \eta \quad (3.77)$$

$$= \int_{\hat{\Omega}} \int_{\mathbb{R}^3} \left\{ (\hat{\mathbf{C}}_h^1)^\top G^{-1} \frac{\hat{f}_h}{\hat{s}_h} \left(\hat{\mathbf{B}}_{fh}^2 \times DF^{-1} \mathbf{v} \right) \right\} \hat{s}_h \sqrt{g} d^3 v d^3 \eta \quad (3.78)$$

$$\approx \sum_{k=1}^K w_k (\hat{\mathbf{C}}_h^1)^\top (\boldsymbol{\eta}_k) G^{-1} (\boldsymbol{\eta}_k) \left(\hat{\mathbf{B}}_{fh}^2(\boldsymbol{\eta}_k) \times DF^{-1}(\boldsymbol{\eta}_k) \mathbf{v}_k \right) \quad (3.79)$$

$$= \mathbf{c}^\top \mathbb{P}^1 \mathbb{W} \bar{G}^{-1} \mathbb{B}_f \bar{D}F^{-1} \mathbf{V}. \quad (3.80)$$

Collecting the terms (3.27), (3.30), (3.29) and (3.28), we find in summary the following semi-discrete momentum balance equation:

$$\mathcal{A} \mathbf{u} = \mathcal{T}^\top \mathbb{C}^\top \mathbb{M}^2 \mathbf{b} + \mathbb{M}^1 \mathcal{P} \mathbf{b} - \mathbb{P}^1 \mathbb{W} \bar{G}^{-1} \mathbb{B}_f \bar{G}^{-1} (\mathbb{P}^1)^\top \mathbf{u} + \mathbb{P}^1 \mathbb{W} \bar{G}^{-1} \mathbb{B}_f \bar{D}F^{-1} \mathbf{V} - \mathbb{M}^1 \mathbb{G} \mathbf{p}. \quad (3.81)$$

Finally, we also write the equations of motion (3.70) of all particles in a compact matrix-vector form:

$$\frac{d\mathbf{H}}{dt} = \bar{D}F^{-1}(\mathbf{H}) \mathbf{V}, \quad (3.82a)$$

$$\frac{d\mathbf{V}}{dt} = (\bar{D}F^{-1}(\mathbf{H}))^\top \left[\mathbb{B}_f(\mathbf{b}, \mathbf{H}) \bar{G}^{-1}(\mathbf{H}) (\mathbb{P}^1)^\top (\mathbf{H}) \mathbf{u} - \mathbb{B}_f(\mathbf{b}, \mathbf{H}) \bar{D}F^{-1}(\mathbf{H}) \mathbf{V} \right]. \quad (3.82b)$$

3.6 Energy and Hamiltonian system

Let us define the discrete energy corresponding to (2.7). We use the same splitting (3.24) for the kinetic energy of the bulk plasma in order to end up with the same matrix \mathcal{A} as in the semi-discrete momentum balance equation (3.81):

$$\begin{aligned} \mathcal{H}_{1h} &:= \frac{1}{4} \int_{\hat{\Omega}} \left[\boldsymbol{\Pi}_1 \left(\frac{\hat{\rho}_{\text{eq}}^3}{\sqrt{g}} \hat{\mathbf{U}}_h^1 \right) \right]^\top G^{-1} \hat{\mathbf{U}}_h^1 \sqrt{g} d^3 \eta + \frac{1}{4} \int_{\hat{\Omega}} \left(\hat{\mathbf{U}}_h^1 \right)^\top G^{-1} \boldsymbol{\Pi}_1 \left(\frac{\hat{\rho}_{\text{eq}}^3}{\sqrt{g}} \hat{\mathbf{U}}_h^1 \right) \sqrt{g} d^3 \eta \\ &\quad + \frac{1}{2} \int_{\hat{\Omega}} (\hat{\mathbf{B}}_h^2)^\top G \hat{\mathbf{B}}_h^2 \frac{1}{\sqrt{g}} d^3 \eta + \frac{1}{\gamma-1} \int_{\hat{\Omega}} \hat{p}_h^0 \sqrt{g} d^3 \eta + \frac{1}{2} \int_{\hat{\Omega}} \int_{\mathbb{R}^3} v^2 f_h d^3 v d^3 x \\ &= \frac{1}{2} \mathbf{u}^\top \mathcal{A} \mathbf{u} + \frac{1}{2} \mathbf{b}^\top \mathbb{M}^2 \mathbf{b} + \frac{1}{\gamma-1} \mathbf{p}^\top \mathbf{n}^0 + \frac{1}{2} \mathbf{V}^\top \mathbb{W} \mathbf{V}. \end{aligned} \quad (3.83)$$

The expression for the energy of the kinetic species (last term) is obtained by using the discrete distribution function (3.68) and evaluating the integrals. The vector \mathbf{n} contains all integrals of each basis function in V_0 over $\hat{\Omega}$, i.e.

$$\mathbf{n}^0 := \left(\int_{\hat{\Omega}} \Lambda_0^0 \sqrt{g} d^3 \eta, \dots, \int_{\hat{\Omega}} \Lambda_{N^0-1}^0 \sqrt{g} d^3 \eta \right)^\top. \quad (3.84)$$

If we collect all finite element coefficients and particle positions in phase space in a single vector $\mathbf{R} := (\boldsymbol{\rho}, \mathbf{u}, \mathbf{p}, \mathbf{b}, \mathbf{H}, \mathbf{V}) \in \mathbb{R}^{N^3+N^1+N^0+N^2+3K+3K}$, we can write the semi-discrete MHD equations (3.10), (3.15), (3.39) and (3.81) and PIC equations (3.82) in the following compact form:

$$\begin{aligned} \frac{d\mathbf{R}}{dt} = \mathbb{J}\nabla_{\mathbf{R}}\mathcal{H}_{1h} + \mathbb{K}\mathbf{R} = & \underbrace{\begin{pmatrix} 0 & 0 & 0 & 0 & 0 & 0 \\ 0 & \mathbb{J}_{11}(\mathbf{b}, \mathbf{H}) & \mathbb{J}_{12} & 0 & 0 & \mathbb{J}_{14}(\mathbf{b}, \mathbf{H}) \\ 0 & 0 & 0 & 0 & 0 & 0 \\ 0 & -\mathbb{J}_{12}^\top & 0 & 0 & 0 & 0 \\ 0 & 0 & 0 & 0 & 0 & \mathbb{J}_{34}(\mathbf{H}) \\ 0 & -\mathbb{J}_{14}^\top(\mathbf{b}, \mathbf{H}) & 0 & 0 & -\mathbb{J}_{34}^\top(\mathbf{H}) & \mathbb{J}_{44}(\mathbf{b}, \mathbf{H}) \end{pmatrix}}_{=: \mathbb{J}} \underbrace{\begin{pmatrix} 0 \\ \mathcal{A}\mathbf{u} \\ 0 \\ \mathbb{M}^2\mathbf{b} \\ 0 \\ \mathbb{W}\mathbf{V} \end{pmatrix}}_{=: \nabla_{\mathbf{R}}\mathcal{H}_{1h}} \\ + \underbrace{\begin{pmatrix} 0 & -\mathbb{D}\mathcal{Q} & 0 & 0 & 0 & 0 \\ 0 & 0 & \mathcal{A}^{-1}\mathbb{M}^1\mathcal{P} & -\mathcal{A}^{-1}\mathbb{M}^1\mathbb{G} & 0 & 0 \\ 0 & (\mathbb{M}^0)^{-1} [\mathbb{G}^\top\mathbb{M}^1\mathcal{S} + (\gamma-1)\mathcal{K}^\top\mathbb{G}^\top\mathbb{M}^1] & 0 & 0 & 0 & 0 \\ 0 & 0 & 0 & 0 & 0 & 0 \\ 0 & 0 & 0 & 0 & 0 & 0 \\ 0 & 0 & 0 & 0 & 0 & 0 \end{pmatrix}}_{=: \mathbb{K}} \underbrace{\begin{pmatrix} \boldsymbol{\rho} \\ \mathbf{u} \\ \mathbf{p} \\ \mathbf{b} \\ \mathbf{H} \\ \mathbf{V} \end{pmatrix}}_{=: \mathbf{R}}. \end{aligned} \quad (3.85)$$

We find that our spatial discretization results in a system which can be written as the sum of a non-canonical Hamiltonian part with the Poisson matrix \mathbb{J} and a non-Hamiltonian part with the matrix \mathbb{K} . As already mentioned in Section 2, the latter only plays a role for compressible waves and if $\nabla \times \mathbf{B}_{\text{eq}} \neq 0$ (then $\mathcal{P} = 0$). In particular, we remark that obtaining the Hamiltonian part relies on the symmetry of \mathcal{A} , \mathbb{M}^2 and \mathbb{W} . In this case $\nabla_{\mathbf{R}}\mathcal{H}_{1h}$ takes the simple form given in the first line of (3.85) and only then the semi-discrete system of equation can be written in the form (3.85). While the symmetry is obvious for the last two matrices (mass matrix and diagonal matrix with particle weights on the diagonal), the symmetry of \mathcal{A} is ensured by the splitting performed in (3.24). The anti-symmetry $\mathbb{J}^\top = -\mathbb{J}$ immediately implies conservation of \mathcal{H}_{1h} for the Hamiltonian part of (3.85):

$$\frac{d}{dt}\mathcal{H}_{1h}(\mathbf{R}(t)) = (\nabla_{\mathbf{R}}\mathcal{H}_{1h})^\top \mathbb{J} \frac{d\mathbf{R}}{dt} = (\nabla_{\mathbf{R}}\mathcal{H}_{1h})^\top \mathbb{J} \nabla_{\mathbf{R}}\mathcal{H}_{1h} = -(\nabla_{\mathbf{R}}\mathcal{H}_{1h})^\top \mathbb{J} \nabla_{\mathbf{R}}\mathcal{H}_{1h} = 0. \quad (3.86)$$

The single blocks of \mathbb{J} are given by

$$\mathbb{J}_{11}(\mathbf{b}, \mathbf{H}) = -\mathcal{A}^{-1}\mathbb{P}^1(\mathbf{H})\mathbb{W}\tilde{\mathcal{G}}^{-1}(\mathbf{H})\mathbb{B}_f(\mathbf{b}, \mathbf{H})\tilde{\mathcal{G}}^{-1}(\mathbf{H})(\mathbb{P}^1)^\top(\mathbf{H})\mathcal{A}^{-1}, \quad (3.87a)$$

$$\mathbb{J}_{12} = \mathcal{A}^{-1}\mathcal{T}^\top\mathbb{C}^\top, \quad (3.87b)$$

$$\mathbb{J}_{14}(\mathbf{b}, \mathbf{H}) = \mathcal{A}^{-1}\mathbb{P}^1(\mathbf{H})\tilde{\mathcal{G}}^{-1}(\mathbf{H})\mathbb{B}_f(\mathbf{b}, \mathbf{H})\tilde{\mathcal{D}}F^{-1}(\mathbf{H}), \quad (3.87c)$$

$$\mathbb{J}_{34}(\mathbf{H}) = \tilde{\mathcal{D}}F^{-1}(\mathbf{H})\mathbb{W}^{-1}, \quad (3.87d)$$

$$\mathbb{J}_{44}(\mathbf{b}, \mathbf{H}) = -(\tilde{\mathcal{D}}F^{-1})^\top(\mathbf{H})\mathbb{B}_f(\mathbf{b}, \mathbf{H})\tilde{\mathcal{D}}F^{-1}(\mathbf{H})\mathbb{W}^{-1}. \quad (3.87e)$$

4 Time discretization

In order to keep the energy conservation property of the Hamiltonian part, we propose two splitting steps: First, to take advantage of (3.86), we split apart the non-Hamiltonian part and solve successively the Hamiltonian part $d\mathbf{R}/dt = \mathbb{J}\nabla_{\mathbf{R}}\mathcal{H}_{1h}$ and non-Hamiltonian part $d\mathbf{R}/dt = \mathbb{K}\mathbf{R}$, and second, we apply Poisson splitting to the Hamiltonian part and solve each (anti-symmetric) sub-step in an energy conserving way. We recall the Hamiltonian part:

$$\frac{d}{dt} \begin{pmatrix} \mathbf{u} \\ \mathbf{b} \\ \mathbf{H} \\ \mathbf{V} \end{pmatrix} = \begin{pmatrix} \mathbb{J}_{11}(\mathbf{b}, \mathbf{H}) & \mathbb{J}_{12} & 0 & \mathbb{J}_{14}(\mathbf{b}, \mathbf{H}) \\ -\mathbb{J}_{12}^\top & 0 & 0 & 0 \\ 0 & 0 & 0 & \mathbb{J}_{34}(\mathbf{H}) \\ -\mathbb{J}_{14}^\top(\mathbf{b}, \mathbf{H}) & 0 & -\mathbb{J}_{34}^\top(\mathbf{H}) & \mathbb{J}_{44}(\mathbf{b}, \mathbf{H}) \end{pmatrix} \begin{pmatrix} \mathcal{A}\mathbf{u} \\ \mathbb{M}^2\mathbf{b} \\ 0 \\ \mathbb{W}\mathbf{V} \end{pmatrix}. \quad (4.1)$$

Splitting the Poisson matrix \mathbb{J} into five separate matrices containing only equally colored blocks and introducing a temporal grid $t_n = n\Delta t$ with $n \in \mathbb{N}_0$ leads to the following sub-steps:

Sub-step 1 The first sub-system reads

$$\dot{\mathbf{u}} = \mathbb{J}_{11}(\mathbf{b}, \mathbf{H})\mathcal{A}\mathbf{u}, \quad \dot{\mathbf{b}} = 0, \quad \dot{\mathbf{H}} = 0, \quad \dot{\mathbf{V}} = 0. \quad (4.2)$$

We solve the equation for \mathbf{u} with the energy-preserving, implicit Crank-Nicolson method [12]. Note that \mathbb{J}_{11} does not change in this step:

$$\mathbf{u}^{n+1} = \mathbf{u}^n + \frac{\Delta t}{2} \mathbb{J}_{11}(\mathbf{b}^n, \mathbf{H}^n) \mathcal{A}(\mathbf{u}^n + \mathbf{u}^{n+1}), \quad (4.3)$$

$$\Leftrightarrow \left(\mathbb{I}_{N^1} - \frac{\Delta t}{2} \mathbb{J}_{11}(\mathbf{b}^n, \mathbf{H}^n) \mathcal{A} \right) \mathbf{u}^{n+1} = \left(\mathbb{I}_{N^1} + \frac{\Delta t}{2} \mathbb{J}_{11}(\mathbf{b}^n, \mathbf{H}^n) \mathcal{A} \right) \mathbf{u}^n. \quad (4.4)$$

To avoid the inversion of the matrix \mathcal{A} , we multiply the second line with \mathcal{A} from the left-hand side to obtain

$$\left(\mathcal{A} - \frac{\Delta t}{2} \mathcal{A} \mathbb{J}_{11}(\mathbf{b}^n, \mathbf{H}^n) \mathcal{A} \right) \mathbf{u}^{n+1} = \left(\mathcal{A} + \frac{\Delta t}{2} \mathcal{A} \mathbb{J}_{11}(\mathbf{b}^n, \mathbf{H}^n) \mathcal{A} \right) \mathbf{u}^n. \quad (4.5)$$

Hence, in every time step, we first assemble the matrix $\mathcal{A} \mathbb{J}_{11}(\mathbf{b}^n, \mathbf{H}^n) \mathcal{A}$ and followed by solving above linear system for \mathbf{u}^{n+1} . We denote the corresponding integrator by $\Phi_{\Delta t}^1 : \mathbb{R}^{N^1} \rightarrow \mathbb{R}^{N^1}$, $\mathbf{u}^n \mapsto \mathbf{u}^{n+1}$.

Sub-step 2 The second sub-system reads

$$\dot{\mathbf{u}} = \mathbb{J}_{12} \mathbb{M}^2 \mathbf{b}, \quad \dot{\mathbf{b}} = -\mathbb{J}_{12}^\top \mathcal{A} \mathbf{u}, \quad \dot{\mathbf{H}} = 0, \quad \dot{\mathbf{V}} = 0. \quad (4.6)$$

As before, we apply the Crank-Nicolson method to obtain

$$\mathbf{u}^{n+1} = \mathbf{u}^n + \frac{\Delta t}{2} \mathcal{A}^{-1} \mathcal{T}^\top \mathbb{C}^\top (\mathbf{b}^n + \mathbf{b}^{n+1}), \quad (4.7)$$

$$\mathbf{b}^{n+1} = \mathbf{b}^n - \frac{\Delta t}{2} \mathbb{C} \mathcal{T} \Delta t (\mathbf{u}^n + \mathbf{u}^{n+1}), \quad (4.8)$$

and solve for \mathbf{u}^{n+1} by plugging the second into the first equation. After some straightforward manipulations this results in the update rules

$$\mathbf{u}^{n+1} = S_2^{-1} \left[\left(\mathcal{A} - \frac{\Delta t^2}{4} \mathcal{T}^\top \mathbb{C}^\top \mathbb{M}^2 \mathbb{C} \mathcal{T} \right) \mathbf{u}^n + \Delta t \mathcal{T}^\top \mathbb{C}^\top \mathbb{M}^2 \mathbf{b}^n \right], \quad (4.9)$$

$$\mathbf{b}^{n+1} = \mathbf{b}^n - \frac{\Delta t}{2} \mathbb{C} \mathcal{T} (\mathbf{u}^n + \mathbf{u}^{n+1}), \quad (4.10)$$

where $S_2 := \mathcal{A} + \Delta t^2 \mathcal{T}^\top \mathbb{C}^\top \mathbb{M}^2 \mathbb{C} \mathcal{T} / 4$ does not change in time. Particularly, we note the explicit update rule for \mathbf{b} which preserves the divergence-free constraint, i.e. $\mathbb{D} \mathbf{b}^{n+1} = \mathbb{D} \mathbf{b}^n$ due to $\mathbb{D} \mathbb{C} = 0$. We denote the corresponding integrator by $\Phi_{\Delta t}^2 : \mathbb{R}^{N^1} \times \mathbb{R}^{N^2} \rightarrow \mathbb{R}^{N^1} \times \mathbb{R}^{N^2}$, $\mathbf{u}^n, \mathbf{b}^n \mapsto \mathbf{u}^{n+1}, \mathbf{b}^{n+1}$.

Sub-step 3 The third sub-system reads

$$\dot{\mathbf{u}} = \mathbb{J}_{14}(\mathbf{b}, \mathbf{H}) \mathbb{W} \mathbf{V}, \quad \dot{\mathbf{b}} = 0, \quad \dot{\mathbf{H}} = 0, \quad \dot{\mathbf{V}} = -\mathbb{J}_{14}^\top(\mathbf{b}, \mathbf{H}) \mathcal{A} \mathbf{u}. \quad (4.11)$$

We solve this system in the same way as before. Since \mathbf{b} and \mathbf{H} do not change in this step, the same is true for the matrix \mathbb{J}_{14} . Hence $\mathbb{J}_{14} = \mathbb{J}_{14}(\mathbf{b}^n, \mathbf{H}^n)$ and we have

$$\mathbf{u}^{n+1} = \mathbf{u}^n + \frac{\Delta t}{2} \mathbb{J}_{14} \mathbb{W} (\mathbf{V}^n + \mathbf{V}^{n+1}), \quad (4.12)$$

$$\mathbf{V}^{n+1} = \mathbf{V}^n - \frac{\Delta t}{2} \mathbb{J}_{14}^\top (\mathbf{u}^n + \mathbf{u}^{n+1}), \quad (4.13)$$

$$\Leftrightarrow \mathbf{u}^{n+1} = S_3^{-1} \left[\left(\mathcal{A} - \frac{\Delta t^2}{4} \mathcal{A} \mathbb{J}_{14} \mathbb{W} \mathbb{J}_{14}^\top \mathcal{A} \right) \mathbf{u}^n + \Delta t \mathcal{A} \mathbb{J}_{14} \mathbb{W} \mathbf{V}^n \right], \quad (4.14)$$

$$\Leftrightarrow \mathbf{V}^{n+1} = \mathbf{V}^n - \frac{\Delta t}{2} \mathbb{J}_{14}^\top \mathcal{A} (\mathbf{u}^n + \mathbf{u}^{n+1}), \quad (4.15)$$

where $S_3 := \mathcal{A} + \Delta t^2 \mathcal{A} \mathbb{J}_{14} \mathbb{W} \mathbb{J}_{14}^\top \mathcal{A} / 4$ which needs to be assembled in each time step. Note that (4.15) is effectively an update rule for a single particle independently from all the other particles. We denote the corresponding integrator by $\Phi_{\Delta t}^3 : \mathbb{R}^{N^1} \times \mathbb{R}^{3K} \rightarrow \mathbb{R}^{N^1} \times \mathbb{R}^{3K}$, $\mathbf{u}^n, \mathbf{V}^n \mapsto \mathbf{u}^{n+1}, \mathbf{V}^{n+1}$.

Sub-step 4 The fourth sub-system reads

$$\dot{\mathbf{u}} = 0, \quad \dot{\mathbf{b}} = 0, \quad \dot{\mathbf{H}} = \bar{D}F^{-1}(\mathbf{H})\mathbf{V}, \quad \dot{\mathbf{V}} = 0. \quad (4.16)$$

Since this step does not play a role for conservation of energy (the discrete Hamiltonian \mathcal{H}_{1h} does not depend on the particle spatial coordinates), we apply to this system a standard fourth order Runge-Kutta scheme and denote the integrator by $\Phi_{\Delta t}^4 : \mathbb{R}^{3K} \times \mathbb{R}^{3K}, \mathbf{H}^n \mapsto \mathbf{H}^{n+1}$. As for (4.15), this update rule applies to every particle independently from all the other particles.

Sub-step 5 The fifth sub-system reads

$$\dot{\mathbf{u}} = 0, \quad \dot{\mathbf{b}} = 0, \quad \dot{\mathbf{H}} = 0, \quad \dot{\mathbf{V}} = \mathbb{J}_{44}(\mathbf{b}, \mathbf{H})\mathbb{W}\mathbf{V}. \quad (4.17)$$

Using once more the Crank-Nicolson method yields

$$\begin{aligned} & \left[\mathbb{I}_K + \frac{\Delta t}{2} (\bar{D}F^{-1}(\mathbf{H}^n))^{\top} \mathbb{B}_f(\mathbf{b}^n, \mathbf{H}^n) \bar{D}F^{-1}(\mathbf{H}^n) \right] \mathbf{V}^{n+1} \\ & = \left[\mathbb{I}_K - \frac{\Delta t}{2} (\bar{D}F^{-1}(\mathbf{H}^n))^{\top} \mathbb{B}_f(\mathbf{b}^n, \mathbf{H}^n) \bar{D}F^{-1}(\mathbf{H}^n) \right] \mathbf{V}^n, \end{aligned} \quad (4.18)$$

which means that in each time step we effectively solve a 3×3 linear system for every particle since in (4.18) always 3 equations corresponding to one particle are independent from all the other equations representing all the other particles. We denote the corresponding integrator by $\Phi_{\Delta t}^5 : \mathbb{R}^{3K} \times \mathbb{R}^{3K}, \mathbf{V}^n \mapsto \mathbf{V}^{n+1}$.

Sub-step 6 (Non-Hamiltonian part) The sixth sub-system reads

$$\dot{\boldsymbol{\rho}} = -\mathbb{D}\mathcal{Q}\mathbf{u}, \quad \mathcal{A}\dot{\mathbf{u}} = -\mathbb{M}^1\mathbb{G}\mathbf{p} + \mathbb{M}^1\mathcal{P}\mathbf{b}, \quad \mathbb{M}^0\dot{\mathbf{p}} = \left[\mathbb{G}^{\top}\mathbb{M}^1\mathcal{S} + (\gamma - 1)\mathcal{K}^{\top}\mathbb{G}^{\top}\mathbb{M}^1 \right] \mathbf{u}, \quad \dot{\mathbf{b}} = 0. \quad (4.19)$$

Defining $\mathbb{L} := \mathbb{G}^{\top}\mathbb{M}^1\mathcal{S} + (\gamma - 1)\mathcal{K}^{\top}\mathbb{G}^{\top}\mathbb{M}^1$ for a shorter notation, we solve this a last time with the Crank-Nicolson method:

$$\boldsymbol{\rho}^{n+1} = \boldsymbol{\rho}^n - \frac{\Delta t}{2} \mathbb{D}\mathcal{Q}(\mathbf{u}^{n+1} + \mathbf{u}^n), \quad (4.20)$$

$$\begin{pmatrix} \mathcal{A} & \frac{\Delta t}{2}\mathbb{M}^1\mathbb{G} \\ -\frac{\Delta t}{2}\mathbb{L} & \mathbb{M}^0 \end{pmatrix} \begin{pmatrix} \mathbf{u}^{n+1} \\ \mathbf{p}^{n+1} \end{pmatrix} = \begin{pmatrix} \mathcal{A} & -\frac{\Delta t}{2}\mathbb{M}^1\mathbb{G} \\ \frac{\Delta t}{2}\mathbb{L} & \mathbb{M}^0 \end{pmatrix} \begin{pmatrix} \mathbf{u}^n \\ \mathbf{p}^n \end{pmatrix} + \begin{pmatrix} \Delta t\mathbb{M}^1\mathcal{P}\mathbf{b}^n \\ 0 \end{pmatrix}. \quad (4.21)$$

Hence, we first compute \mathbf{u}^{n+1} and \mathbf{p}^{n+1} from (4.21) and then $\boldsymbol{\rho}^{n+1}$ from (4.20). Note that (4.20) implies exact conservation of mass due to the same argument as in (3.12), namely that the basis functions in V_3 are all normalized to one on the logical domain $\hat{\Omega}$. Consequently, the discrete mass is just the sum of the coefficients $\boldsymbol{\rho}$ and from (4.20) it follows that

$$\sum_{i=0}^{N^3-1} \rho_i^{n+1} = \sum_{i=0}^{N^3-1} \rho_i^n, \quad (4.22)$$

due to the form of \mathbb{D} containing only 1, -1 and 0. We denote the corresponding integrator by $\Phi_{\Delta t}^6 : \mathbb{R}^{N^3} \times \mathbb{R}^{N^1} \times \mathbb{R}^{N^0} \rightarrow \mathbb{R}^{N^3} \times \mathbb{R}^{N^1} \times \mathbb{R}^{N^0}, \boldsymbol{\rho}^n, \mathbf{u}^n, \mathbf{p}^n \mapsto \boldsymbol{\rho}^{n+1}, \mathbf{u}^{n+1}, \mathbf{p}^{n+1}$.

In summary, in order to go from time t_n to t_{n+1} , we successively apply the six integrators, where it is important to note that the input of the next integrator must be the output of the previous integrator:

$$\Phi_{\Delta t} := \Phi_{\Delta t}^6 \circ \Phi_{\Delta t}^5 \circ \Phi_{\Delta t}^4 \circ \Phi_{\Delta t}^3 \circ \Phi_{\Delta t}^2 \circ \Phi_{\Delta t}^1. \quad (4.23)$$

This first-order composition is known as the Lie-Trotter splitting [34]. We remark, however, that higher-order compositions are available and can be found e.g. in [25].

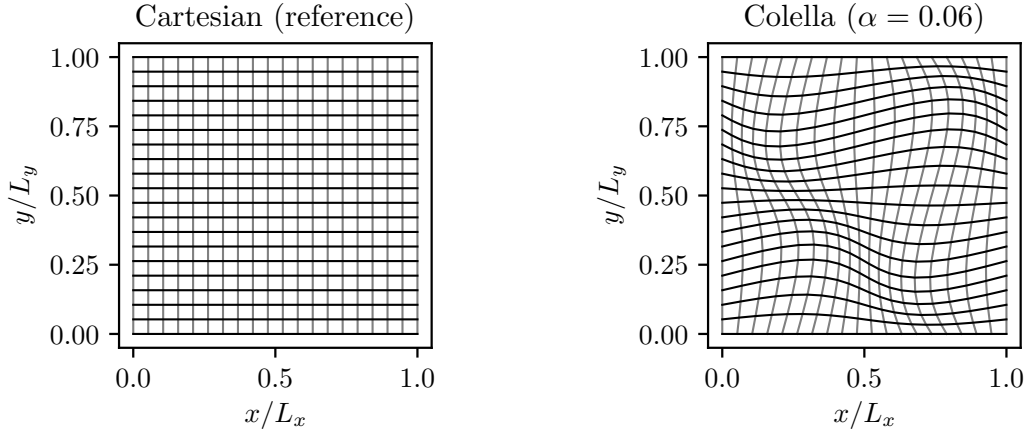


Figure 3: Exemplary meshes in the xy - plane corresponding to the Cartesian mapping (5.1) (left) and Colella mapping (5.2) (right). For the Colella mapping the parameter $\alpha = 0.06$.

5 Numerical experiments

In this section, we present a collection of numerical results obtained with the introduced schemes and methods. We consider two types of mappings \mathbf{F} from the logical domain $\hat{\Omega} = [0, 1]^3$ to the physical domain $\Omega \subset \mathbb{R}^3$. First, a standard Cartesian mapping involving a stretching of the logical cuboid and second, a so-called Colella mapping which additionally involves curved coordinate lines. With the latter, we test the impact of a curved finite element mesh compared to a non-curved, Cartesian mesh:

$$\text{Cartesian : } \mathbf{F} : \hat{\Omega} \rightarrow \Omega, \quad \boldsymbol{\eta} \mapsto \begin{pmatrix} L_x \eta_1 \\ L_y \eta_2 \\ L_z \eta_3 \end{pmatrix} = \mathbf{x}, \quad (5.1)$$

$$\text{Colella : } \mathbf{F} : \hat{\Omega} \rightarrow \Omega, \quad \boldsymbol{\eta} \mapsto \begin{pmatrix} L_x [\eta_1 + \alpha \sin(2\pi\eta_1) \sin(2\pi\eta_2)] \\ L_y [\eta_2 + \alpha \sin(2\pi\eta_2) \sin(2\pi\eta_3)] \\ L_z \eta_3 \end{pmatrix} = \mathbf{x}. \quad (5.2)$$

Here, $L_x, L_y, L_z > 0$ are the side lengths of the rectangular physical domain Ω and $0 \leq \alpha < 1/(2\pi)$ is a dimensionless parameter describing the distortion of the mesh. The upper limit for α is chosen such that the mapping does not become singular anywhere in the domain Ω . Note that all quantities related to the mapping, such as the Jacobian determinant \sqrt{g} or the metric tensor G , are constant and diagonal in case of the Cartesian mapping. Both is not true anymore in case of the Colella mapping. Figure 3 illustrates the resulting coordinate lines in the xy -plane and we note that the Colella mapping coincides with the Cartesian mapping for $\alpha = 0$.

Furthermore, in all simulations shown, we assume a uniform equilibrium bulk plasma in physical space, i.e. the bulk density $\rho_{\text{eq}} = \text{const.}$ and the bulk pressure $p_{\text{eq}} = \text{const.}$. One should keep in mind, however, that e.g. the corresponding 3-form $\hat{\rho}_{\text{eq}}^3 = \sqrt{g} \hat{\rho}_{\text{eq}}$ on the logical domain is not constant in case of the Colella mapping due to the varying Jacobian determinant \sqrt{g} . We perform two classes of numerical tests: The first subsection is concerned with the simulation of linear MHD waves, i.e. we set the contribution from the kinetic ions to zero for all times. The second subsection deals with nonlinear simulations of the interaction of a small population of kinetic ions with shear Alfvén waves. In addition to that, in the third subsection, we provide some information on run times of PIC related parts of the algorithm with current implementation.

5.1 Pure MHD

As previously mentioned, to test the MHD part, we set the contribution from the kinetic ions to zero ($f_h = 0$ for all times) and compare simulated MHD waves to the analytical dispersion relation for waves propagating in x -direction ($\sim \exp(i\mathbf{k}\mathbf{x} - i\omega t)$ with $\mathbf{k} = k\mathbf{e}_x$). Assuming a magnetic field

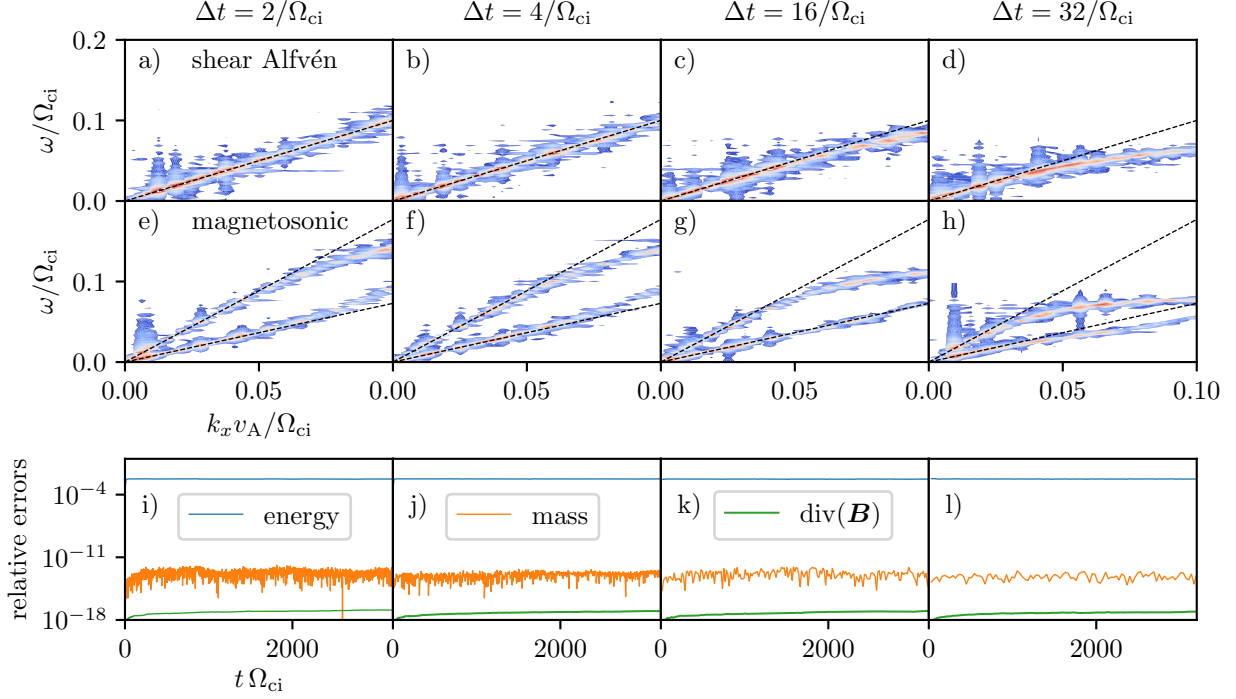


Figure 4: Normalized MHD power spectra in the ω - k_x -plane for different time steps obtained by initialization with random noise. Dashed black lines are the analytical dispersion relations. a)-d) Spectra of the perpendicular component of the velocity field (shear Alfvén wave), e)-h) Spectra of the pressure (magnetosonic waves). i)-l) Time evolution of the total energy (kinetic energy, magnetic energy and internal energy), total mass and $\text{div}(\mathbf{B})$.

$\mathbf{B}_{\text{eq}} = B_{0x}\mathbf{e}_x + B_{0y}\mathbf{e}_y$, the dispersion relation reads

$$\left(\omega^2 - k^2 v_A^2 \frac{B_{0x}^2}{B_{0x}^2 + B_{0y}^2} \right) \left[\omega^2 - \frac{1}{2} k^2 (c_S^2 + v_A^2) (1 \pm \sqrt{1 - \delta}) \right] = 0, \quad \delta = \frac{4B_{0x}^2 c_S^2 v_A^2}{(c_S^2 + v_A^2)^2 (B_{0x}^2 + B_{0y}^2)}, \quad (5.3)$$

where the first term in the round brackets represents the shear Alfvén wave and the second term in the squared brackets the slow (-) and fast (+) magnetosonic (or magneto-acoustic) wave, respectively. The two characteristic velocities are the Alfvén velocity $v_A^2 = (B_{0x}^2 + B_{0y}^2)/(\mu_0 \rho_{\text{eq}})$ and the speed of sound $c_S^2 = \gamma p_{\text{eq}}/\rho_{\text{eq}}$.

To excite waves with multiple wavelengths, we initialize STRUPHY with random noise in the η_1 - η_2 -plane on the logical domain, meaning that we do not compute the initial finite element coefficients from some prescribed initial condition, but we load the initial finite element coefficients $\boldsymbol{\rho}^0$, \mathbf{u}^0 and \mathbf{p}^0 randomly. However, we set the initial coefficients of the magnetic field \mathbf{b}^0 to zero not to violate the divergence-free constraint $\mathbb{D}\mathbf{b}^0 = 0$. Moreover, we set $\beta = 2\mu_0 p_{\text{eq}}/(B_{0x}^2 + B_{0y}^2) = 1$ and $B_{0x} = B_{0y}$ which results in $c_S^2 = \gamma v_A^2/2$. We normalize frequencies to the ion cyclotron frequency Ω_{ci} and velocities to the Alfvén velocity. This results in a normalization of spatial scales to v_A/Ω_{ci} .

We perform two tests: First, for the Cartesian mapping (5.1), we increase the time step Δt in the time integration scheme $\Phi_{\Delta t}$ (4.23) and second, we increase the parameter α for the Colella mapping (5.2) for a fixed time step $\Delta t = 16/\Omega_{ci}$. In both cases we investigate the impact of the parameter variation on the resulting MHD spectra. Fixed numerical parameters are the degrees of the B-splines $p = (3, 3, 1)$, the number of elements $N_{\text{el}} = (80, 80, 2)$, the side lengths $L_x = L_y = 2000 v_A/\Omega_{ci}$ and $L_z = 50$, the number of Gauss-Legendre quadrature points per element for the computation of mass matrices $n_{\text{q,el}} = (6, 6, 2)$, the number of quadrature points per integration interval of histopolations (needed for projections) $n_{\text{q,pr}} = (6, 6, 2)$, the simulation time $T_{\text{end}} = 3200/\Omega_{ci}$ and the usage of periodic boundary conditions. This set of parameters results in a grid spacing on the logical domain of $h = 25 v_A/\Omega_{ci}$ in all three directions. To obtain the wave spectra along the physical x -direction, we

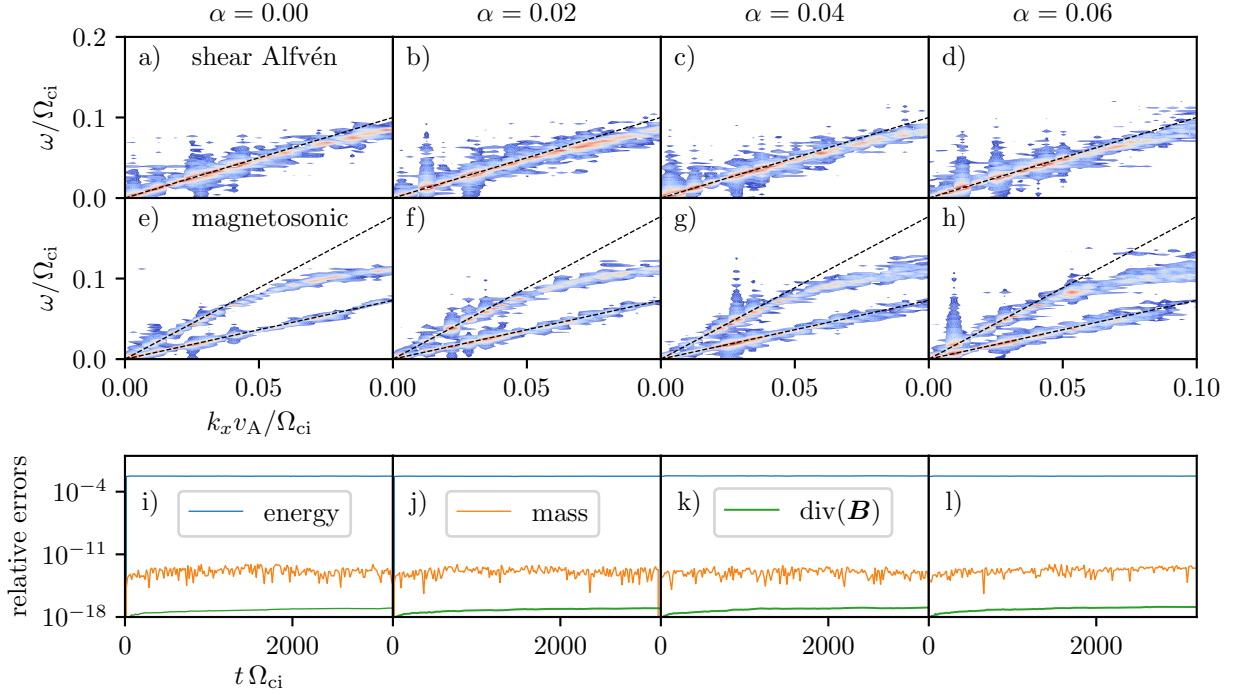


Figure 5: Normalized MHD power spectra in the $\omega - k_x$ -plane for different mesh distortions obtained by initialization with random noise. Dashed black lines are the analytical dispersion relations. a) - d) Spectra of the perpendicular component of the velocity field (shear Alfvén wave), e) - h) Spectra of the pressure (magnetosonic waves). i) - l) Time evolution of the total energy (kinetic energy, magnetic energy and internal energy), total mass and $\text{div}(\mathbf{B})$.

first push-forward the simulation results from the logical domain to physical (x, y, z) -space, followed by performing a three-dimensional discrete Fourier transform in time t and physical coordinates x and y , $(t, x, y) \rightarrow (\omega, k_x, k_y)$. Finally, we plot the squared absolute values of the transformation in the $\omega - k_x$ -plane for $k_y = 0$. With the chosen parameters $k_{x,\text{max}} = \pi/h \approx 0.126 \Omega_{ci}/v_A$.

Figure 4 shows the resulting wave spectra for four time steps $\Delta t = 2/\Omega_{ci}$, $\Delta t = 4/\Omega_{ci}$, $\Delta t = 16/\Omega_{ci}$ and $\Delta t = 32/\Omega_{ci}$. For the first two time steps, the Courant–Friedrichs–Lewy (CFL) number $v_{\text{max}}\Delta t/h < 1$ and for the last two time steps $v_{\text{max}}\Delta t/h > 1$, where $v_{\text{max}} \approx 1.77 v_A$ is the phase velocity of the fastest wave in the system, that is, the fast magnetosonic wave. The numerical stability of the last two runs is ensured by the implicitness of the time integrators $\Phi_{\Delta t}^2$ and $\Phi_{\Delta t}^6$, showing that STRUPHY is not limited by the CFL condition $v_{\text{max}}\Delta t/h < 1$. Moreover, it can be seen that the dispersion relation of the shear Alfvén wave is reproduced very well for all wavelengths and frequencies for the first three time steps and only for the largest time step, there is a significant deviation from the exact dispersion relation, meaning that frequencies $\omega \gtrsim 0.05 \Omega_{ci}$ are not resolved anymore with the time step $\Delta t = 32/\Omega_{ci}$. The simulated spectra corresponding to the two magnetosonic waves show a stronger sensitivity to the chosen time step. While frequencies up to $\omega \approx 0.15 \Omega_{ci}$ are properly resolved for $\Delta t = 2/\Omega_{ci}$, this is true up to $\omega \approx 0.04 \Omega_{ci}$ for $\Delta t = 32/\Omega_{ci}$. We expect that higher frequencies are better resolved for a fixed time step if one also uses a higher-order splitting scheme in time, based on the propagators $\Phi_{\Delta t}^n$ ($n = 1, \dots, 6$). The current implementation is only high-order in space. In addition to the wave spectra, we show in Figure 4 on the bottom the time evolution of the relative errors in the conservation of the total energy, (kinetic energy + internal energy + magnetic energy), the divergence of the magnetic field and the relative error in the conservation of the total mass. The maximum errors are approximately for the divergence $1 \cdot 10^{-17}$, for the mass $1 \cdot 10^{-12}$ and for the energy $5 \cdot 10^{-3}$, where the latter is due to the non-Hamiltonian part in the semi-discrete system of equations (3.85). If this non-Hamiltonian part was zero, the energy would also be conserved at machine precision, due to the skew-symmetry of the matrix \mathcal{J} . This will be the case for the shear Alfvén wave shown in the next section.

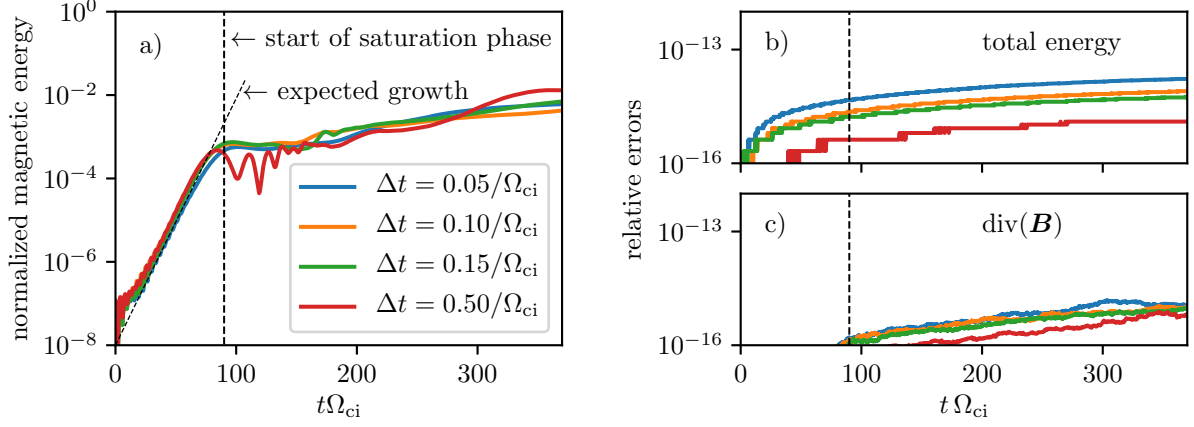


Figure 6: Interaction of a shear Alfvén wave with full-orbit kinetic, energetic ions: a) Time evolution of the normalized magnetic field energy for different time steps. b) Corresponding evolution of the relative error in the conservation of the total energy (bulk kinetic, magnetic, bulk internal and energetic ion kinetic and internal energy). c) Corresponding evolution of the divergence of the magnetic field.

In Figure 5, we take the Colella mapping (5.2) and vary the distortion parameter α for a fixed time step $\Delta t = 16 \Omega_{ci}$, meaning that the CFL number $v_{\max} \Delta t / h > 1$ for all simulations. The only visible impact appears for $\alpha = 0.04$ and $\alpha = 0.06$ at wavenumbers $k \gtrsim 0.07 \Omega_{ci} / v_A$, where we observe a "broadening" of the dispersion branch especially for the fast magnetosonic wave. Since there are only very few elements per wavelength in this region, the distortion seems to worsen the spatial accuracy. However, because there is already a deviation due to the time resolution, this is not problematic. Finally, the mesh distortion does not impact the time evolution of the three conserved quantities showing that the expected conservation properties of our scheme hold independently of the chosen mesh and metric.

5.2 Wave-particle resonance

Here, we include kinetic, energetic ions with an initially ($t = 0$) isotropic, shifted Maxwellian distribution function of the form

$$f_h(\mathbf{x}, \mathbf{v}, t = 0) = \frac{n_h}{\pi^{3/2} v_{th}^{3/2}} \exp\left(-\frac{(v_x - v_0)^2 + v_y^2 + v_z^2}{v_{th}^2}\right). \quad (5.4)$$

Moreover, we choose a uniform background magnetic field in x -direction $\mathbf{B}_{eq} = B_0 \mathbf{e}_x$. It is straightforward to show that the distribution function (5.4) is a valid choice for an equilibrium state since it results in a current $\mathbf{J}_{h,eq} = n_h v_0 \mathbf{e}_x$ pointing in x -direction such that $\mathbf{J}_{h,eq} \times \mathbf{B}_{eq} = 0$. For parallel wave propagation ($\mathbf{k} = k \mathbf{e}_x$), the fully linearized system exhibits the dispersion relation

$$D_{R/L}(k, \omega) = \omega^2 - v_A^2 k^2 \pm \nu_h \omega \Omega_{ci} + \nu_h \Omega_{ci}^2 \frac{\omega - kv_0}{kv_{th}} Z\left(\frac{\omega - kv_0 \pm \Omega_{ci}}{kv_{th}}\right), \quad (5.5)$$

where $\nu_h = n_h m_i / \rho_{eq}$ is the ratio of the equilibrium bulk and energetic ion mass densities, $\Omega_{ci} = eB_0 / m_i$ the ion cyclotron frequency, R/L denote right- and left-handed circularly polarized waves, respectively, and Z denotes the plasma dispersion function [17]

$$Z(\xi) = \sqrt{\pi} e^{-\xi^2} \left(i - \frac{2}{\sqrt{\pi}} \int_0^\xi e^{t^2} dt \right) = \sqrt{\pi} e^{-\xi^2} (i - \operatorname{erfi}(\xi)). \quad (5.6)$$

Note that in the absence of energetic ions ($\nu_h = 0$) the dispersion relation coincides with the dispersion relation of shear Alfvén waves. Numerically solving the dispersion relation for parameters $k = 0.8 \Omega_{ci} / v_A$, $v_{th} = v_A$, $v_0 = 2.5 v_A$ and $\nu_h = 0.05$ yields for the R-wave an expected real frequency $\omega_r \approx 0.8012 \Omega_{ci}$ and a positive growth rate (imaginary part) $\omega_i \approx 0.0681 \Omega_{ci}$ caused by an

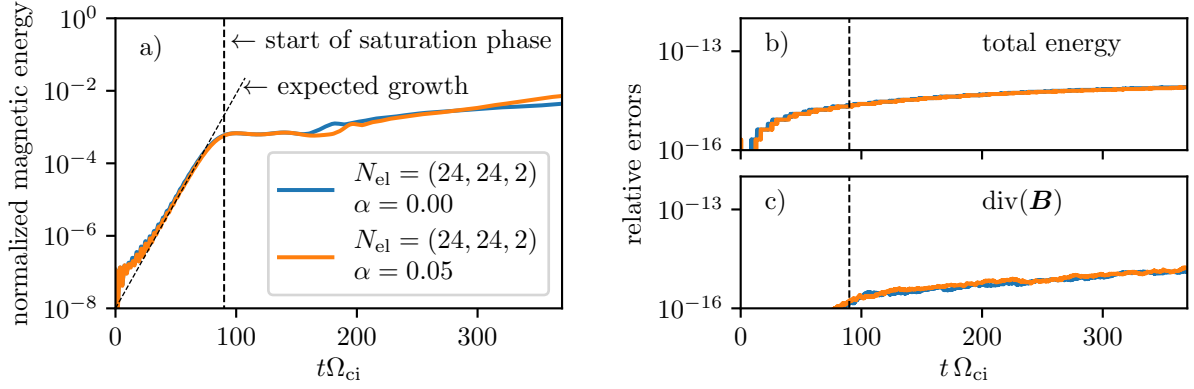


Figure 7: Interaction of a shear Alfvén wave with full-orbit kinetic, energetic ions: a) Time evolution of the normalized magnetic field energy for different mesh resolution and metric. b) Corresponding evolution of the relative error in the conservation of the total energy (bulk kinetic, magnetic, bulk internal and energetic ion kinetic and internal energy). c) Corresponding evolution of the divergence of the magnetic field.

energy transfer to the shear Alfvén wave from energetic ions having velocities v_x in the vicinity of the resonant velocity $v_R = (\omega_r + \Omega_{ci})/k \approx 2.25 v_A$. Physically, the resonant velocity is the Doppler shifted wave phase velocity, where the Doppler shift is caused by the ion cyclotron motion. The choice $k = 0.8 \Omega_{ci}/v_A$ is purely for testing purposes since according to (5.5) $kv_A/\Omega_{ci} \ll 1$ does not result in an unstable mode in slab geometry. We fix these physical parameters in the following. To excite the instability for a single wave number, we chose the initial magnetic field $\mathbf{B}(\mathbf{x}, t = 0) = 10^{-3} \sin(kx) \mathbf{e}_z$, which corresponds to the excitation of a shear Alfvén wave. Fixed numerical parameters are the degrees of the B-splines $p = (2, 2, 1)$, the side lengths $L_x = L_y = 2\pi/k$ and $L_z = 1 v_A/\Omega_{ci}$, the number of Gauss-Legendre quadrature points per element for the computation of mass matrices $n_{q,el} = (6, 6, 2)$, the number of quadrature points per integration interval of histopolations (needed for projections) $n_{q,pr} = (6, 6, 2)$, the simulation time $T_{end} = 370/\Omega_{ci}$ and the usage of periodic boundary conditions. Furthermore, for the PIC part, we load the particles’ logical coordinates uniformly random and the particles’ velocities normally random (including the shift v_0 in v_x -direction) using standard random number generators, such that the initial sampling density and particle weights are given by

$$\bar{s}_h^0(\boldsymbol{\eta}, \mathbf{v}) = \frac{1}{\pi^{3/2} v_{th}^{3/2}} \exp\left(-\frac{(v_x - v_0)^2 + v_y^2 + v_z^2}{v_{th}^2}\right), \quad (5.7)$$

$$\Rightarrow w_k = \frac{\hat{f}_h^0(\boldsymbol{\eta}_k^0, \mathbf{v}_k^0) \sqrt{g}(\boldsymbol{\eta}_k^0)}{K \bar{s}_h^0(\boldsymbol{\eta}_k^0, \mathbf{v}_k^0)} = \frac{n_h \sqrt{g}(\boldsymbol{\eta}_k^0)}{K}. \quad (5.8)$$

Therefore, the particle weights are all the same in case of the Cartesian mapping but not in case of the Colella mapping with $\alpha \neq 0$ due to the varying Jacobian determinant \sqrt{g} .

In order to demonstrate the energy conservation property of the temporally discretized semi-discrete Hamiltonian system (4.1), we artificially switch off the time integrator $\Phi_{\Delta t}^6$ corresponding to the non-Hamiltonian part, i.e. we set $\Phi_{\Delta t}^6 = \text{id}$. Since we simulate a shear Alfvén wave not involving pressure perturbations, this choice is physically meaningful. For the first run, we use the number of elements $N_{el} = (16, 16, 2)$, a Cartesian mesh and a rather large number of particles $K = 8 \cdot 10^6$, corresponding to 15625 particles per cell, and vary the time step Δt which we expect to be in the inverse ion cyclotron frequency range due to the simulated physics being a cyclotron interaction. Note that the instability can also be simulated with much fewer particles as will be shown later. In Figure 6, we show on the left-hand side the resulting evolution of the magnetic field energy with respect to time for four different time steps. Qualitatively, we observe an exponential growth phase followed by a saturation phase at $t \approx 90/\Omega_{ci}$. The numerical growth rates of all runs show good agreement with the analytical expectations from the dispersion relation (5.5) and all runs are numerically stable. However, the largest time step of Δt shows large oscillations at the onset of the saturation phase.

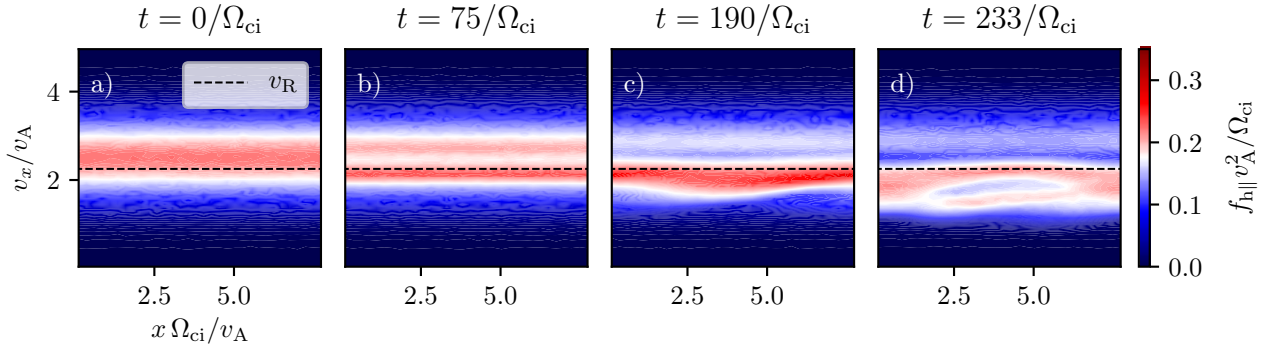


Figure 8: Interaction of a shear Alfvén wave with full-orbit kinetic, energetic ions: Energetic ion distribution function in the $x - v_x$ -plane at four different times. Dashed black line indicates the resonant velocity. a) initial condition, b) exponential growth phase, c) - d) saturation phase.

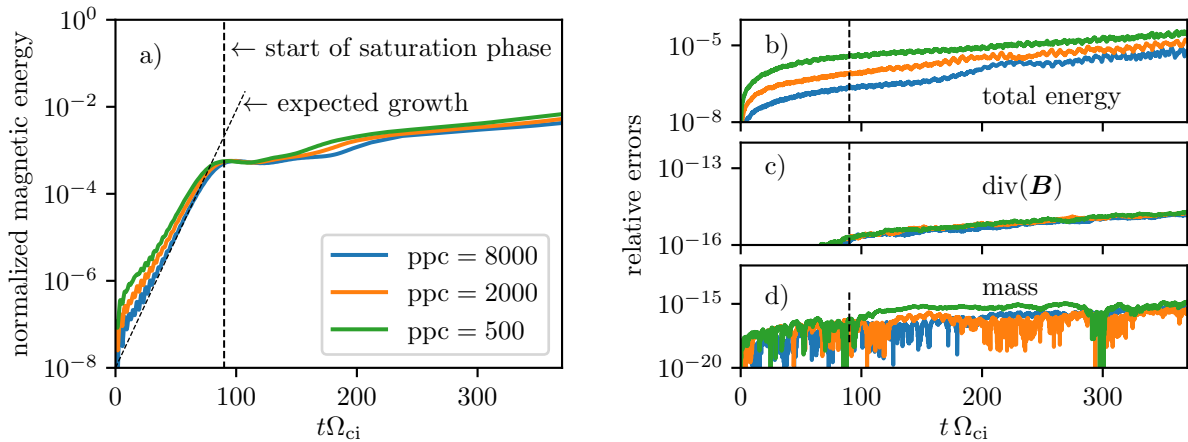


Figure 9: Interaction of a shear Alfvén wave with full-orbit kinetic, energetic ions with non-Hamiltonian part tuned on: a) Time evolution of the normalized magnetic field energy for three different numbers of particles per cell (ppc). b) Corresponding evolution of the relative error in the conservation of the total energy (bulk kinetic, magnetic, bulk internal and energetic ion kinetic and internal energy). c) Corresponding evolution of the divergence of the magnetic field. d) Corresponding evolution of the total mass.

Hence we deduce that the ion cyclotron interaction is not properly resolved in this case. Nevertheless, we observe in Figure 6 on the right-hand side an energy error of the order 10^{-14} throughout the whole simulation. The same is true for the divergence-free constraint of the magnetic field with an error of the order 10^{-15} . Also the mass, not shown here, is conserved exactly.

For the second set of runs, we set the time step $\Delta t = 0.10/\Omega_{ci}$, increase the number of elements to $N_{el} = (24, 24, 2)$ while leaving all other parameters unchanged, followed by additionally distorting the finite element mesh by using the Colella mapping (5.2) with distortion parameter $\alpha = 0.05$. The two results are displayed in Figure 7. We observe the same behavior of the evolution of the relative errors in the conservation of the total energy and the divergence-free constraint proving that our scheme conserves these quantities independently of the chosen mesh and metric (or mapping \mathbf{F}).

In Figure 8, we additionally show the partially cumulative distribution function of the energetic ions

$$f_{h\parallel}(x, v_x) = \int_0^{L_z} \int_0^{L_y} \int_{-\infty}^{\infty} \int_{-\infty}^{\infty} f_h dv_y dv_z dy dz, \quad (5.9)$$

at four different times obtained by accumulating particle weights on a 32×64 binning grid in $x - v_x$ -space. We identify the initial condition at $t = 0/\Omega_{ci}$, namely a uniform distribution along x and a Maxwellian distribution along v_x centered at $v_0 = 2.5 v_A$. At $t = 75/\Omega_{ci}$ we observe that particles

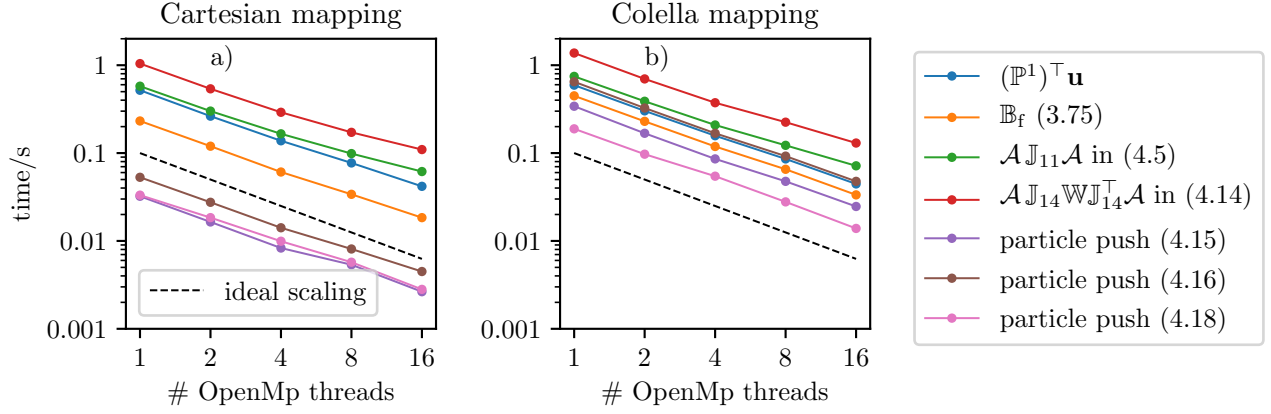


Figure 10: Run times of PIC related parts of the time integrator $\Phi_{\Delta t}$ (4.23) dependent on the number of OpenMP threads. The number of particles $K = 1 \cdot 10^5$ and number of elements $N_{\text{el}} = (16, 16, 2)$. a) For the Cartesian mapping (5.1). b) For the Colella mapping (5.2).

having velocities close to the resonant velocity v_R loose energy which gradually shifts the maximum of the distribution function below v_R . Hence energy is transferred to the shear Alfvén wave. At $t = 190/\Omega_{ci}$, which is already in the saturation phase, a perturbation in x -direction starts to form which finally leads to a phase space hole visible at $t = 233/\Omega_{ci}$.

As a last run, we include the time integrator $\Phi_{\Delta t}^6$ corresponding to the non-Hamiltonian part. We set $\Delta t = 0.05/\Omega_{ci}$, $N_{\text{el}} = (16, 16, 2)$ and use the Colella mapping with $\alpha = 0.05$. The results are shown in Figure 9. For the blue curve we used $K = 4 \cdot 10^6$ particles with corresponds to ≈ 8000 particles per cell (ppc). We observe on the right-hand side of Figure Figure 9 that the total energy is not conserved to machine precision anymore, but the error is bounded below 10^{-6} . Although we are simulating a shear Alfvén wave which should be non-perturbative in pressure, the particle noise leads to small pressure perturbations which worsens the energy conservation property. To show that the error is caused by particle noise, we run the same test case with reduced numbers of particles (2000 and 500 particles per cell) and indeed we observe that the error increases. Qualitatively, we also observe that 500 particles per cell is in principle enough for this particular test case as mentioned earlier. The only remarkable difference appears in the very beginning of a simulation namely that a small number of particles leads to a nonphysical jump in the magnetic field energy caused by the increased noise level. In this case the analytical growth rate is not captured correctly but the saturation dynamics remains unchanged.

5.3 Runtime of PIC routines

Finally, we measure elapsed times of chosen parts of our time integration scheme $\Phi_{\Delta t}$ (4.23) involving the particles. To these belong the evaluation of the components of the discrete 1-form velocity field and the discrete 2-form magnetic field at the particle positions (that is, computing $(\mathbb{P}^1)^T(\mathbf{H}^n) \mathbf{u}$ and \mathbb{B}_f at some time t_n), the assembly of the matrices $\mathcal{A} \mathbb{J}_{11}(\mathbf{b}^n, \mathbf{H}^n) \mathcal{A}$ and $\mathcal{A} \mathbb{J}_{14} \mathbb{W} \mathbb{J}_{14}^T \mathcal{A}$ for the integrators $\Phi_{\Delta t}^1$ and $\Phi_{\Delta t}^3$, respectively, and the three particle updates in $\Phi_{\Delta t}^3$, $\Phi_{\Delta t}^4$ and $\Phi_{\Delta t}^5$. We perform measurements for the Cartesian and Colella mapping (5.1) and (5.2), respectively, and for different numbers of OpenMP threads. We use $K = 1 \cdot 10^5$ particles and take the average of 100 time steps. The resulting times are shown in Figure 10. We note that the most time consuming parts are the particle accumulations (green and red curve). Furthermore, we see the impact of the spline degree on the elapsed times since the evaluation of a 1-form (blue curve) is more expensive than the evaluation of a 2-form. The latter involves the evaluation of more D-splines compared to B-splines whereas the opposite is true for a 1-form. Finally, we see that the chosen mapping has a considerable impact on the performance especially for the three particle pushing steps (purple, brown and pink curves) as the Colella mapping requires the evaluation of a sin-function which is not the case for the Cartesian mapping.

As we increase the number of OpenMp threads, we obtain an almost optimal strong scaling behavior, meaning that the elapsed times are halved if the number of threads is doubled.

6 Conclusion

We presented the new hybrid MHD-kinetic code STRUPHY which solves linearized, ideal MHD equations, coupled nonlinearly to fully kinetic 6d Vlasov equations in curved geometries. The algorithm provably conserves mass, energy and $\nabla \cdot \mathbf{B} = 0$ irrespective of metric, grid spacing, chosen spline degree and degree of time splitting, c.f. the update rules (4.20) for the mass, (4.10) for the magnetic field, and the skew-symmetry of the matrix in (4.1) which is subjected to Poisson splitting. We demonstrated this behaviour for a Cartesian mapping and the Colella mapping, depicted in Figure 3, by verifying dispersion relations for MHD (no kinetic species) and resonant MHD (current coupling) test cases. The current version of STRUPHY features an OpenMp parallelisation of the kinetic PIC part, which allows the distribution of particles on up to 40 threads on a single node on the available computing cluster. However, no considerable effort has been put into performance optimisation yet. Having proved in this work the feasibility of our approach, further development steps include:

1. Implementation of an OpenMp/MPI hybrid parallelisation: linear systems in the splitting steps 1-6 of Section 4 will be solved by iterative methods with single-node parallelisation (up to 40 threads). Particle equations will be subjected to MPI for multi-node communication.
2. Implementation of a drift-kinetic particle pusher for the simulation of low-frequency phenomena. The suitable Hamiltonian model has been developed in [8].
3. Creation of an interface to MHD equilibrium codes such as VMEC [21] for the purpose of loading realistic tokamak and stellarator equilibria.
4. Extension to nonlinear MHD and implementation of a pressure coupling scheme.

Some of these efforts are already on the way. Once the OpenMp/MPI hybrid parallelisation is in place, we aim to perform benchmark studies with other hybrid codes mentioned in the introduction. Ultimately, we believe that STRUPHY brings several new qualities to the already existing arsenal of hybrid codes, in particular:

- the exact conservation properties guarantee long-time stability,
- the high-order methods guarantee accuracy,
- the implicitness enables large time steps in the MHD part, jumping over high-frequencies,
- the use of full MHD provides the possibility of exploring the whole range of MHD waves.

In the future, these features can make STRUPHY an attractive alternative also to fully kinetic simulations of energetic particle effects.

Acknowledgments

We would like to thank Yaman Güçlü and Said Hadjout for constantly helping us with implementation details and code acceleration. Moreover, we thank Ahmed Ratnani for introducing us to the construction of local commuting projectors as well as Eric Sonnendrücker, Florian Hindenlang and Cesare Tronci for general input and useful discussions throughout this work.

This work has been carried out within the framework of the Eurofusion Consortium and has received funding from the Euratom research and training programme 2014-2018 and 2019-2020 under grant agreement No 633053. The views and opinions expressed herein do not necessarily reflect those of the European Commission.

Appendix A Formulae for exterior calculus of differential forms

A.1 Exterior product

The exterior (or wedge) product $a^p \wedge b^q$ relates a p -form and a q -form to a $(p+q)$ -form. In terms of the components \hat{a}^p (respectively \hat{a}^p) and \hat{b}^q (resp. \hat{b}^q), it is given by

$$\wedge : \Lambda^p(\Omega) \times \Lambda^q(\Omega) \rightarrow \Lambda^{p+q}(\Omega), \quad \begin{cases} \hat{a}^0, \hat{b}^q \mapsto \hat{a}^0 \hat{b}^q, & p = 0, q \in \{0, 1, 2, 3\}, \\ \hat{a}^1, \hat{b}^1 \mapsto \hat{a}^1 \times \hat{b}^1, & p = 1, q = 1, \\ \hat{a}^1, \hat{b}^2 \mapsto (\hat{a}^1)^\top \hat{b}^2, & p = 1, q = 2, \\ \hat{a}^3, \hat{b}^q \mapsto 0, & p = 3, q \in \{0, 1, 2, 3\}, \end{cases} \quad (\text{A.1})$$

which are all possible cases due to the anti-symmetry $a^p \wedge b^q = (-1)^{pq} b^q \wedge a^p$.

A.2 Interior product

The interior product $i_a a^p$ relates a vector field \mathbf{a} and a p -form a^p to a $(p-1)$ -form. In terms of the components $\hat{\mathbf{a}}$ and \hat{a}^p (resp. $\hat{\mathbf{a}}^p$), it is given by

$$i_a : \Lambda^p(\Omega) \times T\Omega \rightarrow \Lambda^{p-1}(\Omega), \quad \begin{cases} \hat{a}^0, \hat{\mathbf{a}} \mapsto 0, & p = 0, \\ \hat{a}^1, \hat{\mathbf{a}} \mapsto (\hat{a}^1)^\top \hat{\mathbf{a}}, & p = 1, \\ \hat{a}^2, \hat{\mathbf{a}} \mapsto \hat{a}^2 \times \hat{\mathbf{a}}, & p = 2, \\ \hat{a}^3, \hat{\mathbf{a}} \mapsto \hat{a}^3 \hat{\mathbf{a}}, & p = 3. \end{cases} \quad (\text{A.2})$$

A.3 Hodge-star operator

The Hodge-star operator $*a^p$ relates a p -form a^p to a $(3-p)$ -form. In terms of the components \hat{a}^p (resp. $\hat{\mathbf{a}}^p$), it is given by

$$* : \Lambda^p(\Omega) \rightarrow \Lambda^{3-p}(\Omega), \quad \begin{cases} \hat{a}^0 \mapsto \sqrt{g} \hat{a}^0, & p = 0, \\ \hat{a}^1 \mapsto \sqrt{g} G^{-1} \hat{a}^1, & p = 1, \\ \hat{a}^2 \mapsto \frac{1}{\sqrt{g}} G \hat{a}^2, & p = 2, \\ \hat{a}^3 \mapsto \frac{1}{\sqrt{g}} \hat{a}^3, & p = 3. \end{cases} \quad (\text{A.3})$$

A.4 Exterior derivative

The exterior derivative da^p acts on the components of p -forms \hat{a}^p (resp. $\hat{\mathbf{a}}^p$) as the grad, div and curl on scalar fields and components of vector fields in Cartesian coordinates (see Table 2).

$d : \Lambda^p(\Omega) \rightarrow \Lambda^{p+1}(\Omega)$	$p = 0$	$p = 1$	$p = 2$	$p = 3$
	$\hat{a}^0 \mapsto \hat{\nabla} \hat{a}^0$	$\hat{\mathbf{a}}^1 \mapsto \hat{\nabla} \times \hat{\mathbf{a}}^1$	$\hat{\mathbf{a}}^2 \mapsto \hat{\nabla} \cdot \hat{\mathbf{a}}^2$	$\hat{a}^3 \mapsto 0$

Table 2: Exterior derivative in terms of the components \hat{a}^p (resp. $\hat{\mathbf{a}}^p$).

Moreover, the exterior derivative satisfies

$$1) \quad d(a^p + b^p) = da^p + db^p, \quad (\text{A.4a})$$

$$2) \quad d(a^p \wedge b^q) = da^p \wedge b^q + (-1)^p a^p \wedge db^q \quad (\text{Leibniz rule}), \quad (\text{A.4b})$$

$$3) \quad dda^p = 0. \quad (\text{A.4c})$$

A.5 Hilbert spaces of p -forms

The Hilbert spaces of p -forms are defined as

$$L^2\Lambda^p(\Omega) := \{a^p \in \Lambda^p(\Omega) : (a^p, a^p) < \infty\}, \quad (\text{A.5a})$$

$$H\Lambda^p(\Omega) := \{a^p \in L^2\Lambda^p(\Omega), da^p \in L^2\Lambda^{p+1}(\Omega)\}, \quad (\text{A.5b})$$

and equipped with the following scalar product (or L^2 -inner product):

$$(\cdot, \cdot) : \Lambda^p(\Omega) \times \Lambda^p(\Omega) \rightarrow \mathbb{R}, \quad (a^p, b^p) := \int_{\Omega} a^p \wedge *b^p = \begin{cases} \int_{\hat{\Omega}} \hat{a}^0 \hat{b}^0 \sqrt{g} d^3\eta, & p = 0, \\ \int_{\hat{\Omega}} (\hat{a}^1)^\top G^{-1} \hat{b}^1 \sqrt{g} d^3\eta, & p = 1, \\ \int_{\hat{\Omega}} (\hat{a}^2)^\top G \hat{b}^2 \frac{1}{\sqrt{g}} d^3\eta, & p = 2, \\ \int_{\hat{\Omega}} \hat{a}^3 \hat{b}^3 \frac{1}{\sqrt{g}} d^3\eta, & p = 3. \end{cases} \quad (\text{A.6})$$

Note the symmetry $(a^p, b^p) = (b^p, a^p)$ of the scalar product. Due to the property (A.4c) of the exterior derivative, the Hilbert spaces of p -forms form the chain complex

$$H\Lambda^0(\Omega) \xrightarrow{d} H\Lambda^1(\Omega) \xrightarrow{d} H\Lambda^2(\Omega) \xrightarrow{d} L^2\Lambda^3(\Omega), \quad (\text{A.7})$$

with the property that the image of the previous operator is in the kernel of the next operator.

A.6 Co-differential operator

Using generalized Stokes' theorem

$$\int_{\Omega} da^p = \int_{\partial\Omega} a^p, \quad (\text{A.8})$$

together with Leibniz rule (A.4b) and $** = \text{id}$, we can derive the formal adjoint of the exterior derivative via

$$\begin{aligned} (da^{p-1}, b^p) &= \int_{\Omega} da^{p-1} \wedge *b^p \\ &= \int_{\Omega} d(a^{p-1} \wedge *b^p) - (-1)^{p-1} \int_{\Omega} a^{p-1} \wedge d(*b^p) \\ &= \int_{\partial\Omega} a^{p-1} \wedge *b^p + (-1)^p \int_{\Omega} a^{p-1} \wedge **d(*b^p) \\ &= \int_{\partial\Omega} a^{p-1} \wedge *b^p + (-1)^p (a^{p-1}, *d * b^p). \end{aligned} \quad (\text{A.9})$$

The operator

$$d^* : \Lambda^p(\Omega) \rightarrow \Lambda^{p-1}(\Omega), \quad a^p \mapsto d^* a^p = (-1)^p * d * a^p, \quad (\text{A.10})$$

is called the *co-differential* operator.

Appendix B δf -method

The δf -method is a common approach for noise reduction in PIC codes. The main assumption is that the unknown distribution function f_h remains close to some known distribution function. It is typically but not necessarily the equilibrium distribution function $f_{h,\text{eq}}$ for which (ideally) analytical moments in velocity space

$$\rho_{h,\text{eq}} = \int_{\mathbb{R}^3} f_{h,\text{eq}} d^3v, \quad \mathbf{J}_{h,\text{eq}} = \int_{\mathbb{R}^3} \mathbf{v} f_{h,\text{eq}} d^3v, \quad (\text{B.1})$$

are available. Therefore, only the perturbed part of the distribution function is integrated the particle positions in phase space. Using $f_h = (f_h - f_{h,\text{eq}}) + f_{h,\text{eq}}$, we modify (3.71)-(3.73) in the following way:

$$\begin{aligned} \text{CC}(\rho_h) &\approx \int_{\hat{\Omega}} \int_{\mathbb{R}^3} \left\{ (\hat{\mathbf{C}}_h^1)^\top G^{-1} \frac{\hat{f}_h - \hat{f}_{h,\text{eq}}}{\hat{s}_h} \left(\hat{\mathbf{B}}_{fh}^2 \times G^{-1} \hat{\mathbf{U}}_h^1 \right) \right\} \hat{s}_h \sqrt{g} d^3v d^3\eta \\ &\quad + \int_{\hat{\Omega}} (\hat{\mathbf{C}}_h^1)^\top G^{-1} \hat{\rho}_{h,\text{eq}} \left(\hat{\mathbf{B}}_{fh}^2 \times G^{-1} \hat{\mathbf{U}}_h^1 \right) \sqrt{g} d^3\eta \end{aligned} \quad (\text{B.2})$$

$$\begin{aligned} &\approx \sum_{k=1}^K \frac{1}{K} \underbrace{\left(\frac{\hat{f}_h^0(\boldsymbol{\eta}_k^0, \mathbf{v}_k^0)}{\hat{s}_h^0(\boldsymbol{\eta}_k^0, \mathbf{v}_k^0)} - \frac{\hat{f}_{h,\text{eq}}(\boldsymbol{\eta}_k, \mathbf{v}_k)}{\hat{s}_h^0(\boldsymbol{\eta}_k^0, \mathbf{v}_k^0)} \right)}_{=: w_k(\boldsymbol{\eta}_k(t), \mathbf{v}_k(t))} (\hat{\mathbf{C}}_h^1)^\top(\boldsymbol{\eta}_k) G^{-1}(\boldsymbol{\eta}_k) \left(\hat{\mathbf{B}}_{fh}^2(\boldsymbol{\eta}_k) \times G^{-1}(\boldsymbol{\eta}_k) \hat{\mathbf{U}}_h^1(\boldsymbol{\eta}_k) \right) \\ &\quad + \mathbf{c}^\top \int_{\hat{\Omega}} \Lambda^1 \frac{\hat{\rho}_{h,\text{eq}}}{\sqrt{g}} \mathbb{B}^G(\Lambda^1)^\top d^3\eta \mathbf{u} \end{aligned} \quad (\text{B.3})$$

$$= \mathbf{c}^\top \mathbb{P}^1 \mathbb{W} \bar{G}^{-1} \mathbb{B}_f \bar{G}^{-1} (\mathbb{P}^1)^\top \mathbf{u} + \mathbf{c}^\top \mathbb{X}^1(\mathbf{b}) \mathbf{u}. \quad (\text{B.4})$$

Hence we get two modifications compared to the full- f description: First, the particle weights are not constant anymore but depend on the particle positions in phase space. Second, we get an additional term with the weighted mass matrix $\mathbb{X}^1(\mathbf{b})$, where \mathbb{B}^G denotes once more the cross-product in terms of a matrix-vector product as in (3.16) but built from the three components of $G \hat{\mathbf{B}}_{fh}^2 = G(\hat{\mathbf{B}}_{\text{eq}}^2 + \mathbf{b}^\top \Lambda^2)$. In the same way, we obtain for the term involving the current density

$$\text{CC}(\mathbf{J}_h) \approx \mathbf{c}^\top \mathbb{P}^1 \mathbb{W} \bar{G}^{-1} \mathbb{B}_f \bar{D} \bar{F}^{-1} \mathbf{V} + \mathbf{c}^\top \int_{\hat{\Omega}} \Lambda^1 \frac{1}{\sqrt{g}} \left[(G \hat{\mathbf{B}}_{fh}^2) \times (G \hat{\mathbf{J}}_{h,\text{eq}}) \right] d^3\eta \quad (\text{B.5})$$

$$= \mathbf{c}^\top \mathbb{P}^1 \mathbb{W} \bar{G}^{-1} \mathbb{B}_f \bar{D} \bar{F}^{-1} \mathbf{V} + \mathbf{c}^\top \mathbf{x}(\mathbf{b}), \quad (\text{B.6})$$

where it is important to note that $\hat{\mathbf{J}}_{h,\text{eq}}$ are the components of the vector field (and not 2-form) corresponding to the equilibrium current density. Regarding our time stepping scheme, we simply add the new terms in sub-steps 1 and 3, respectively, and solve in the same way for \mathbf{u}^{n+1} (sub-step 1) and $\mathbf{u}^{n+1}, \mathbf{V}^{n+1}$ (sub-step 3) as before using the Crank-Nicolson method. Moreover, we assume the weights to be constant in sub-step 3. In the end of a time step we then update the weights according to (B.3). However, this method breaks the energy conservation property of the Hamiltonian part, since we loose the anti-symmetry of the Poisson matrix.

Appendix C Weights in quasi spline interpolation

	$\omega^i (p=2)$	$\omega^i (p=3)$
clamped		$\{1, 0, 0, 0, 0\}, \quad i=0$
	$\{1, 0, 0\}, \quad i=0$	$\{-\frac{5}{18}, \frac{40}{18}, -\frac{24}{18}, \frac{8}{18}, -\frac{1}{18}\}, \quad i=1$
	$\{-\frac{1}{2}, 2, -\frac{1}{2}\}, \quad 0 < i < \hat{n}_N - 1$	$\{\frac{1}{6}, -\frac{8}{6}, \frac{20}{6}, -\frac{8}{6}, \frac{1}{6}\}, \quad 1 < i < \hat{n}_N - 2$
	$\{0, 0, 1\}, \quad i = \hat{n}_N - 1$	$\{-\frac{1}{18}, \frac{8}{18}, -\frac{24}{18}, \frac{40}{18}, -\frac{5}{18}\}, \quad i = \hat{n}_N - 2$
		$\{0, 0, 0, 0, 1\}, \quad i = \hat{n}_N - 1$
periodic	$\{-\frac{1}{2}, 2, -\frac{1}{2}\}, \quad \forall i$	$\{\frac{1}{6}, -\frac{8}{6}, \frac{20}{6}, -\frac{8}{6}, \frac{1}{6}\}, \quad \forall i$

Table 3: The weights ω^i in (3.58) for the interpolator I^p for quadratic ($p=2$) and cubic ($p=3$) B-splines, respectively.

	$\tilde{\omega}^i (p = 2)$	$\tilde{\omega}^i (p = 3)$
clamped	$\{\frac{3}{2}, -\frac{1}{2}, 0\}, \quad i = 0$	$\{\frac{23}{18}, -\frac{17}{18}, \frac{7}{18}, -\frac{1}{18}, 0, 0\}, \quad i = 0$
	$\{-\frac{1}{2}, \frac{3}{2}, \frac{3}{2}, -\frac{1}{2}\}, \quad 0 < i < \hat{n}_D - 1$	$\{-\frac{8}{18}, \frac{56}{18}, -\frac{28}{18}, \frac{4}{18}, 0, 0\}, \quad i = 1$
	$\{0, -\frac{1}{2}, \frac{3}{2}\}, \quad i = \hat{n}_D - 1$	$\{\frac{3}{18}, -\frac{21}{18}, \frac{36}{18}, \frac{36}{18}, -\frac{21}{18}, \frac{3}{18}\}, \quad 1 < i < \hat{n}_D - 2$
		$\{0, 0, \frac{4}{18}, -\frac{28}{18}, \frac{56}{18}, -\frac{8}{18}\}, \quad i = \hat{n}_D - 2$
		$\{0, 0, -\frac{1}{18}, \frac{7}{18}, -\frac{17}{18}, \frac{23}{18}\}, \quad i = \hat{n}_D - 1$
periodic	$\{-\frac{1}{2}, \frac{3}{2}, \frac{3}{2}, -\frac{1}{2}\}, \quad \forall i$	$\{\frac{3}{18}, -\frac{21}{18}, \frac{36}{18}, \frac{36}{18}, -\frac{21}{18}, \frac{3}{18}\}, \quad \forall i$

Table 4: The weights $\tilde{\omega}^i$ in (3.62) for the histopolator H^{p-1} for quadratic ($p = 2$) and cubic ($p = 3$) B-splines, respectively.

References

- [1] D. Arnold, R. Falk, and R. Winther. Finite element exterior calculus: from Hodge theory to numerical stability. *Bulletin of the American mathematical society*, 47(2):281–354, 2010.
- [2] D. N. Arnold. *Finite element exterior calculus*, volume 93. SIAM, 2018.
- [3] D. N. Arnold, R. S. Falk, and R. Winther. Finite element exterior calculus, homological techniques, and applications. *Acta numerica*, 15:1–155, 2006.
- [4] A. Y. Aydemir. A unified monte carlo interpretation of particle simulations and applications to non-neutral plasmas. *Physics of Plasmas*, 1(4):822–831, 1994.
- [5] E. Belova, R. Denton, and A. Chan. Hybrid simulations of the effects of energetic particles on low-frequency MHD waves. *Journal of Computational Physics*, 136(2):324–336, 1997.
- [6] S. Briguglio, G. Vlad, F. Zonca, and C. Kar. Hybrid magnetohydrodynamic-gyrokinetic simulation of toroidal Alfvén modes. *Physics of Plasmas*, 2(10):3711–3723, 1995.
- [7] A. Buffa, G. Sangalli, and R. Vázquez. Isogeometric analysis in electromagnetics: B-splines approximation. *Computer Methods in Applied Mechanics and Engineering*, 199:1143–1152, 03 2010.
- [8] J. W. Burby and C. Tronci. Variational approach to low-frequency kinetic-MHD in the current coupling scheme. *Plasma Physics and Controlled Fusion*, 59(4):045013, 2017.
- [9] W. Burtis and R. Helliwell. Magnetospheric chorus: Occurrence patterns and normalized frequency. *Planetary and Space Science*, 24(11):1007 – 1024, 1976.
- [10] G. Chen and L. Chacón. An energy-and charge-conserving, nonlinearly implicit, electromagnetic 1D-3V Vlasov–Darwin particle-in-cell algorithm. *Computer Physics Communications*, 185(10):2391–2402, 2014.
- [11] L. Chen and F. Zonca. Physics of Alfvén waves and energetic particles in burning plasmas. *Reviews of Modern Physics*, 88(1):015008, 2016.
- [12] J. Crank and P. Nicolson. A practical method for numerical evaluation of solutions of partial differential equations of the heat-conduction type. *Mathematical Proceedings of the Cambridge Philosophical Society*, 43(1):50–67, 1947.
- [13] C. de Boor and G. Fix. Spline approximation by quasiinterpolants. *Journal of Approximation Theory*, 8(1):19 – 45, 1973.

- [14] E. Evstatiev and B. Shadwick. Variational formulation of particle algorithms for kinetic plasma simulations. *Journal of Computational Physics*, 245:376–398, 2013.
- [15] G. Farin. *Curves and Surfaces for Computer-Aided Geometric Design*. Academic Press, 1993.
- [16] T. Frankel. *The Geometry of Physics: An Introduction*. Cambridge University Press, 3 edition, 2011.
- [17] B. D. Fried and S. D. Conte. *The Plasma Dispersion Function*. Academic Press, 1961.
- [18] Y. He, H. Qin, Y. Sun, J. Xiao, R. Zhang, and J. Liu. Hamiltonian time integrators for Vlasov-Maxwell equations. *Physics of Plasmas*, 22(12):124503, 2015.
- [19] Y. He, Y. Sun, H. Qin, and J. Liu. Hamiltonian particle-in-cell methods for Vlasov-Maxwell equations. *Physics of Plasmas*, 23(9):092108, 2016.
- [20] W. Heidbrink. Basic physics of Alfvén instabilities driven by energetic particles in toroidally confined plasmas. *Physics of Plasmas*, 15(5):055501, 2008.
- [21] S. P. Hirshman and J. C. Whitson. Steepest-descent moment method for three-dimensional magnetohydrodynamic equilibria. *The Physics of Fluids*, 26(12):3553–3568, 1983.
- [22] A. Könies, S. Briguglio, N. Gorelenkov, T. Fehér, M. Isaev, P. Lauber, A. Mishchenko, D. Spong, Y. Todo, W. Cooper, et al. Benchmark of gyrokinetic, kinetic MHD and gyrofluid codes for the linear calculation of fast particle driven TAE dynamics. *Nuclear Fusion*, 58(12):126027, 2018.
- [23] M. Kraus, K. Kormann, P. J. Morrison, and E. Sonnendrücker. GEMPIC: Geometric electromagnetic particle-in-cell methods. *Journal of Plasma Physics*, 83(4), 2017.
- [24] P. Lauber. Super-thermal particles in hot plasmas—Kinetic models, numerical solution strategies, and comparison to tokamak experiments. *Physics Reports*, 533(2):33–68, 2013.
- [25] R. I. McLachlan and G. R. W. Quispel. Splitting methods. *Acta Numerica*, 11:341–434, 2002.
- [26] P. J. Morrison. Structure and structure-preserving algorithms for plasma physics. *Physics of Plasmas*, 24(5):055502, 2017.
- [27] P. J. Morrison and J. M. Greene. Noncanonical Hamiltonian density formulation of hydrodynamics and ideal magnetohydrodynamics. *Physical Review Letters*, 45(10):790, 1980.
- [28] W. Park, E. Belova, G. Fu, X. Tang, H. Strauss, and L. Sugiyama. Plasma simulation studies using multilevel physics models. *Physics of Plasmas*, 6(5):1796–1803, 1999.
- [29] H. Qin, J. Liu, J. Xiao, R. Zhang, Y. He, Y. Wang, Y. Sun, J. W. Burby, L. Ellison, and Y. Zhou. Canonical symplectic particle-in-cell method for long-term large-scale simulations of the Vlasov-Maxwell equations. *Nuclear Fusion*, 56(1):014001, 2015.
- [30] O. Santolík, D. A. Gurnett, J. S. Pickett, M. Parrot, and N. Cornilleau-Wehrin. A microscopic and nanoscopic view of storm-time chorus on 31 march 2001. *Geophysical Research Letters*, 31(2), 2004.
- [31] J. Squire, H. Qin, and W. M. Tang. Geometric integration of the Vlasov-Maxwell system with a variational particle-in-cell scheme. *Physics of Plasmas*, 19(8):084501, 2012.
- [32] Y. Todo and T. Sato. Linear and nonlinear particle-magnetohydrodynamic simulations of the toroidal Alfvén eigenmode. *Physics of plasmas*, 5(5):1321–1327, 1998.
- [33] C. Tronci. Hamiltonian approach to hybrid plasma models. *Journal of Physics A: Mathematical and Theoretical*, 43(37):375501, 2010.

- [34] H. F. Trotter. On the product of semi-groups of operators. *Proc. Am. Math. Soc.*, 10(4):545–551, 1959.
- [35] B. T. Tsurutani and E. J. Smith. Postmidnight chorus: A substorm phenomenon. *Journal of Geophysical Research (1896-1977)*, 79(1):118–127, 1974.
- [36] X. Wang, S. Briguglio, L. Chen, C. Di Troia, G. Fogaccia, G. Vlad, and F. Zonca. An extended hybrid magnetohydrodynamics gyrokinetic model for numerical simulation of shear Alfvén waves in burning plasmas. *Physics of Plasmas*, 18(5):052504, 2011.
- [37] J. Xiao and H. Qin. Field theory and a structure-preserving geometric particle-in-cell algorithm for drift wave instability and turbulence. *Nuclear Fusion*, 59(10):106044, 2019.
- [38] J. XIAO, H. QIN, and J. LIU. Structure-preserving geometric particle-in-cell methods for Vlasov-Maxwell systems. *Plasma Science and Technology*, 20(11):110501, sep 2018.
- [39] J. Xiao, H. Qin, J. Liu, and R. Zhang. Local energy conservation law for a spatially-discretized Hamiltonian Vlasov-Maxwell system. *Physics of Plasmas*, 24(6):062112, 2017.